A 3D Darcy-scale reactive transport modeling of experimental wormhole formation in limestone under geological CO_2 storage conditions

Atefeh Vafaie[1*], Josep M. Soler[2], Jordi Cama[2], Iman R. Kivi[1], Victor Vilarrasa[3]

[1]Department of Earth Science and Engineering, Imperial College London, London, UK

[2]Institute of Environmental Assessment and Water Research, Spanish National Research Council (IDAEA-CSIC), Barcelona, Spain

[3]Mediterranean Institute for Advanced Studies (IMEDEA), Spanish National Research Council (CSIC), Esporles, Spain

[*]Corresponding author: Atefeh Vafaie (a.vafaie@imperial.ac.uk)

Manuscript submitted to the *International Journal of Greenhouse Gas Control* for peer review.

Abstract

Geologic CO_2 storage is projected to play a key role in mitigating the climate change crisis. Changes in pore structure and hydraulic properties are likely to occur in carbonate rocks when they interact with CO_2 as an acid-producing agent, potentially affecting CO_2 flow and storage behavior in the subsurface. Here, we combine laboratory experiments and numerical simulations of CO_2-saturated water and HCl solution injections into limestone specimens to develop an improved understanding of reactive flow in these rocks. We employ a digital rock approach based on X-ray micro-computed tomography (μCT) to construct heterogeneous rock permeability maps, fed as inputs into 3D Darcy-scale reactive transport models of the experiments. The simulations satisfactorily reproduce measured changes in effluent chemistry, porosity and permeability as well as the observed dissolution features in reacted rock samples. The complete dissociation of HCl as

a strong acid results in compact dissolution, numerically captured using the classical Kozeny-Carman porosity-permeability relationship. In contrast, the partial dissociation of aqueous CO_2 as a weak acid and the related pH-buffering effect drive strong feedback between fluid flow and dissolution, leading to wormhole formation. This dissolution pattern can be only reproduced by a large exponent (15 to 27.6) in the porosity-permeability relationship. We show that dimensionless Péclet and Damköhler numbers alone cannot predict the observed dissolution patterns in the rock. The obtained results highlight the primary control of small-scale heterogeneities and acid type on coupled flow and chemical reactions in permeable limestones and the need for a rigorous upscaling approach for field-scale studies.

Keywords:

Carbon capture and storage, rock heterogeneity, fluid-rock interaction, reactive transport modeling, digital rock

1. Introduction

Rapid dissolution of carbonate minerals, primarily calcite and dolomite, in contact with acidic fluids, is of critical significance in various geo-energy operations (Gaus et al., 2010; Gray et al., 2018). Such alterations have been intentionally targeted for acid stimulation of hydrocarbon reservoirs by HCl injection (McLeod, 1984; Fredd and Fogler, 1998), while they may inevitably take place during geologic CO_2 storage where CO_2 dissolution in the resident brine forms carbonic acid (H_2CO_3) (Metz et al., 2005; Gaus et al., 2010; Rohmer et al., 2016; Vafaie et al., 2023a). Field observations have shown that mineral dissolution can cause changes in the pore structure, and thus in the permeability and flow behavior in carbonate reservoirs. For instance, in the SACROC (Scurry Area Canyon Reef Operating Committee) hydrocarbon field, the most productive CO_2 enhanced oil recovery field in the US, mineral dissolution during a CO_2-EOR operation resulted

in 50% injectivity enhancement (Kane et al., 1979). Carbonate reservoirs are widespread in the world and constitute several candidate reservoirs for underground CO_2 storage (Gray, 2015). Assessment of dissolution-induced alterations in carbonate rocks could thus improve our understanding and prediction of storage capacity and flow in these reservoirs (Daccord et al., 1989; Menke et al., 2015; Gray et al., 2021).

Carbonate rocks are significantly heterogeneous over small length scales (Fitch et al., 2015). These heterogeneities are relevant to fluid-rock interactions occurring principally at the pore scale (Steefel, 2008). Heterogeneities in the pore space and mineral distribution control potential fluid flow pathways and the initial extent and location of the mineral-fluid interface available for chemical reactions (Li et al., 2008; Noiriel et al., 2009; Mostaghimi et al., 2010). Earlier experimental studies focused on carbonate rock dissolution consistently showed that heterogeneities play a key role in the development of dissolution patterns in these rocks (Fredd and Fogler, 1998; Noiriel et al., 2005; Ott et al., 2012; Smith et al., 2013; Luquot et al., 2014; Vialle et al., 2014; Gray et al., 2018; Menke et al., 2017; Leger et al., 2022). While stable dissolution fronts have been observed in a few homogeneous carbonate rocks subjected to CO_2-rich solution injection (Smith et al., 2013; Menke et al., 2017), unstable dissolution patterns, particularly in the form of wormholes were found to be prevalent in heterogeneous rocks over a wide range of flow and reaction conditions (Fredd and Fogler, 1998; Ellis et al., 2011; Khather et al., 2022). Insights from X-ray micro-computed tomography (μCT) probing dissolution patterns in rocks point to the initiation of wormholes in regions of high porosity and permeability (Ott and Odai, 2015; Menke et al., 2016). The localization of flow and reactions in heterogeneous rock structures could attenuate effective reaction rates, i.e., the amount of dissolved mineral over a time period (Salehikhoo and Li, 2015; Pereira Nunes et al., 2016). For instance, Al-Khulaifi et al. (2017)

found that reaction rates in a carbonate core reacted with CO_2-rich water are one order of magnitude smaller than the respective batch reaction values. These experimental observations render the dissolution of carbonate rocks a complex interplay between chemical reactions, flow and transport phenomena that has yet to be fully understood.

Numerical simulations have been extensively employed to capture key features of reactive transport and chemical reactions in carbonate rocks (Golfier et al., 2001, 2002; Szymczak and Ladd, 2009, 2011; Hao et al., 2013; Garcia-Rios et al., 2015, 2017; Smith et al., 2017; Hao et al., 2019; Dávila et al., 2020). Breakthroughs in digital rock physics and the ability to develop accurate realizations of the rock microstructure have enabled pore-scale reactive transport modeling in cm-long rock samples (Beckingham et al., 2013; Menke et al., 2015; Soulaine et al., 2018; Noiriel and Soulaine, 2021). Solving chemical reactions coupled with fluid flow (Navier-Stokes equation) and conservation of mass, these modeling approaches accredit strong impacts of small-scale heterogeneities on the progress of flow and dissolution regimes (Li et al., 2008; Beckingham, 2017). The simulations also unravel the critical role of flow and reaction conditions, including the relative importance of diffusion, advection and reaction in the evolution of dissolution patterns in the rock (Kang et al., 2003). Importantly, slow advection relative to mineral dissolution, such as in underground CO_2 storage, favors instabilities in the dissolution front (Menke et al., 2016). Although pore-network modeling can be theoretically implemented at varying scales, their application to large scales is prohibitively resource-intensive (Molins et al., 2014). Thus, macroscale continuum models grounded on Darcy flow approximations are useful alternatives to pore-scale approaches owing to their lower computational cost (Golfier et al., 2001, 2002; Hao et al., 2013, 2019; Smith et al., 2017).

Continuum models manifest the microscopic distribution of mineral composition and pore structure, i.e, volume and surface area, through heterogeneous distributions of macroscopic parameters such as porosity, permeability, mineral dissolution kinetics, and reactive surface area, besides appropriate relationships to account for their evolution with chemical reactions. Physical and chemical behaviors are averaged or homogenized over representative elementary volumes (REVs) (Steefel et al., 2005; Jackson et al., 2020). A typical approach for this task is the application of statistical methods to add random noise to the effective characteristics of the porous medium (Golfier et al., 2002; Panga et al., 2005; Liu and Liu, 2016). Perturbations are commonly applied to the rock permeability controlling the flow field (Golfier et al., 2002; Vialle et al., 2013). A more physically sound approach relies on processing μCT images to parameterize centimeter-scale continuum models (Hao et al., 2013, 2019; Smith et al., 2017; De Paulo Ferreira et al., 2020). Constructing digital rock models is straightforward for porosity and even for the geometric surface area as they involve summing up the total pore volume and the mineral-pore contact surface area over numerical grids, respectively (Jackson et al., 2020; Noiriel et al., 2009; Al-Khulaifi et al., 2017). In contrast, correlating the permeability map with the pore space distribution requires the knowledge of individual pore geometry, pore network connectivity and upscaling through pore-scale simulations (Golfier et al., 2002; Beckingham et al., 2013; Hao et al., 2019). To circumvent this obstacle, Hao et al. (2013) and Smith et al. (2017) considered simplified, uniform distributions of permeability in three discrete rock regions diagnosed from SEM images. Nevertheless, this partitioning approach may introduce further uncertainties into numerical models and become complicated in arbitrary rock structures, specifically when different permeability zones are closely clustered or overlapped.

Porosity is widely considered the best macroscopic descriptor of the pore space complexities and thus, a reliable proxy for permeability estimations in continuum models (Hommel et al., 2018). Porosity-permeability relationships are critical components of continuum reactive transport modeling as they couple fluid flow and the pore structure and serve as practical means to predict flow at larger scales (Hao et al., 2019; Menke et al., 2021). These relationships can be verified and calibrated against high-resolution pore-network modeling (e.g., Beckingham, 2017; Menke et al., 2021) or laboratory acid injection experiments (e.g., Noiriel et al., 2005; Luquot and Gouze, 2009; Smith et al., 2013; Menke et al., 2016). Although power laws frequently best fit the observations, the fitted exponents are uncertain, affecting the ability of continuum models to accurately capture fluid-rock interactions (Smith et al., 2013; Hao et al., 2019). While smaller power values (n = 6-8) were found to capture wormhole formation in a number of carbonate rocks (Hao et al., 2013; Menke et al., 2017), larger values (n = 75) have been reported for some other samples injected with CO_2-rich water (Noiriel et al., 2005; Vialle et al., 2014; Garing et al., 2015). The reason for this large variability remains unclear and central to a better understanding of reactive transport in carbonate formations and the prediction of the ensuing changes in flow properties.

We here bring together flow-through experiments and Darcy-scale numerical simulations of CO_2-saturated water and HCl-solution injections into cm-long limestone cores to provide an improved understanding of coupled flow and reaction leading to dissolution-induced changes of flow properties in this rock. To this end, we directly integrate digital rock models into a 3D continuum-scale reactive transport model (see the methodological overview in Fig. 1). The modeling approach considers an initially homogenous porosity distribution with heterogeneity exclusively applied on the permeability map. We show that through proper parameterization, the Darcy-scale model can predict the evolution of effluent chemistry and capture the formation of observed dissolution

patterns. We rely on simulation results to (1) discuss the effects of the acid type and pore space heterogeneity on dissolution processes and (2) highlight the essential role of heterogeneities in the permeability field on acid-rock interactions. The proposed numerical approach, although simple, captures the underlying physics of reactive transport in carbonate rocks and sets the ground for developing reliable upscaling methods.

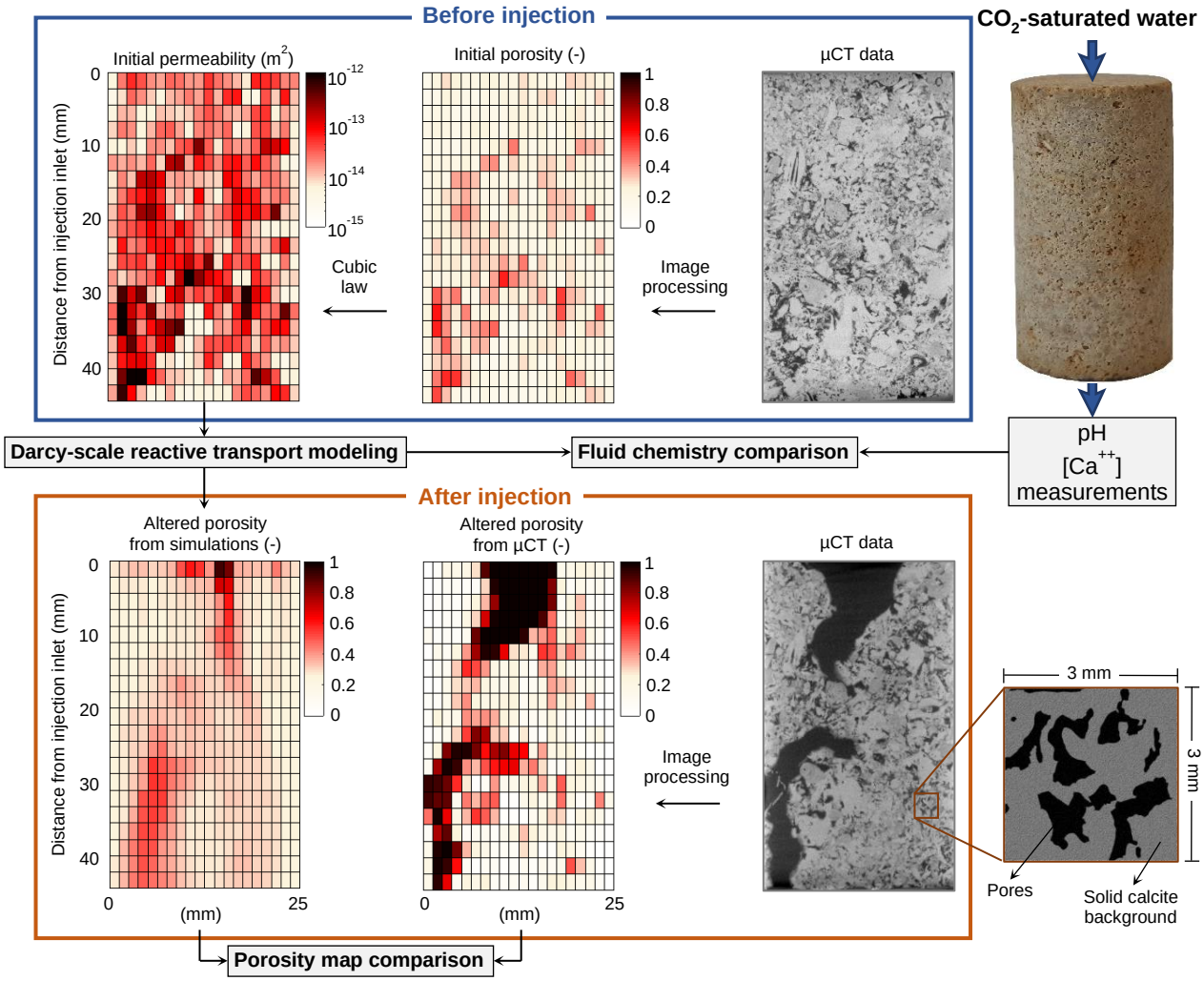

Fig. 1. Overview of the workflow and data used. The grayscale images illustrate µCT scans of a core before and after flooding with acidic solutions. Top-right inside the box: µCT image before injection. Top-middle and Top-left: initial porosity and permeability maps from image processing and a power-law porosity-permeability relationship, respectively. Bottom-right inside the box:

145 µCT image after injection. Bottom-middle and bottom-left dissolution patterns inferred from
146 image processing and continuum-scale reactive transport modeling, respectively (illustrating an
147 example for the specimen flooded with CO_2-rich water).

148

149 **2. Materials and methods**

150 2.1. Sample characterization

151 Two cylindrical cores of grain-supported Pont du Gard Limestone (L_1 and L_2), composed purely
152 of calcite, are used in this study. The cores have a diameter of 25 mm and a length of 44 mm (L_1)
153 and 78 mm (L_2). The basic single-phase flow properties of the samples are measured before and
154 after percolation experiments. The total porosity (ϕ_{bulk}) is calculated as $\phi_b = 1 - \rho_b/\rho_s$ where ρ_b
155 is the bulk dry density of the cores obtained from mass and volume measurements and ρ_s is the
156 skeleton density (i.e., the density of the calcite grains including isolated pores, 2.65 g/cm^3). ρ_s is
157 obtained from the mercury intrusion capillary pressure (MICP) test conducted on a small fragment
158 of the intact Pont du Gard Limestone (see Vafaie et al., 2023b for details). Micro-CT imaging at a
159 resolution of around 20 µm is also performed to characterize pore space distributions and an
160 imaging-based estimate of rock porosity, referred to as $\phi_{\mu CT}$. Permeability is measured using a
161 classic column experiment in accordance with Darcy´s law (Darcy, 1856)

162 $$k = \mu LQ/S\rho gH \quad (1)$$

163 where k (m^2), S (m^2), and L (m) are the intrinsic permeability, cross-section area, and length of the
164 cores, respectively, g (9.81 m/s^2) is gravity acceleration, μ (kg/m/s) is the dynamic fluid viscosity
165 and ρ (kg/m^3) is the fluid density. Q (m^3/s) denotes the steady-state flow rate of fluid through the
166 core, and H (m) is the hydraulic head. Water is used as the working fluid. It should be noted that

the high permeability of the rock causes a pressure drop along the core smaller than the resolution of the pressure transducers (0.1 bar) mounted in flow-through setups. Therefore, permeability changes can not be monitored during the experiments.

2.2. Flow-through experiments

Two percolation experiments with two different experimental setups are performed. A short description of the experiments is given here. More details on the experimental setups can be found in Vafaie et al. (2023b). The experiments are labeled by the rock sample name (L_1 or L_2), injected acidic solution (CO_2 or HCl) and duration of the experiment (28 days).

CO_2-saturated (Milli-Q) water (P_{CO2} = 100 bar and T = 60 ± 2 °C) is injected into the initially water-saturated sample L_1 using a constant flow rate of 0.15 mL/min for 28 days. At these pressure and temperature, a total CO_2 concentration of 1.03 mol/L in Milli-Q water yielding a pH of 3.13 is calculated using the PhreeqC code and PhreeqC database (Parkhurst and Appelo, 2013). The experiment is stopped after 14 days to measure the altered core porosity and permeability. Thereafter, the injection is resumed and the experiment runs for another 14 days under the same experimental conditions. Porosity and permeability are measured again after 28 days.

In the second experiment, two HCl solutions are injected into water-saturated sample L_2 in two consecutive stages at the same flow rate (0.15 mL/min) and temperature (T = 60 ± 2 °C) as in the CO_2 experiment, under atmospheric pressure (P = 1 bar) conditions. The first stage lasts for 17 days and the injected HCl solution is made by adding 3.79 mL of 1 M HCl to 5 L of Milli-Q water to yield a pH similar to that of the injected CO_2-rich water (pH of ~ 3.13). In the second stage, a more acidic HCl solution (pH of 2.66) is injected for 11 days while keeping other experimental conditions constant. A comparison between the results of the two stages is useful to examine the pH effect on limestone dissolution. The pH of the input and output solutions is only measured

during the HCl experiments. The high PCO_2 in the CO_2 experiment prevented accurate measurement of pH due to degassing. A Thermo Scientific Orion Dual Star pH meter is used for pH measurement in the HCl experiment. pH is calibrated at 60°C using standard pH 2, 7, and 9 buffer solutions with a pH uncertainty of 0.02 pH units.

In all experiments, the output solutions are collected periodically (≈ 24 h) and immediately filtered and acidifed (9.90 mL of output aliquots + 0.1 mL of 65% HNO3). The Ca concentration as a result of calcite dissolution is measured using Inductively Coupled Plasma-Atomic Emission Spectrometry (ICP-AES) using a Perkin Elmer Optima 8300. The Ca detection limit and the analytical uncertainty are 6.3×10^{-6} M and 3%, respectively. It should be noted that in both sets of experiments, the water-saturated samples are kept under a constant temperature of 60 °C for 24 hours prior to the injection of acidic solutions to ensure that the initial pore fluid is equilibrated with calcite.

Given that Pont du Gard Limestone only contains calcite, the output Ca concentration is used to calculate the porosity increase ($\Delta\phi$) as

$$\Delta\phi = M_{ca} \cdot \bar{V}_{ca}/V_c \quad (2)$$

where V_c and $\bar{V}_{ca}$ are the volume of the core and calcite molar volume, respectively, and M_{Ca} is the number of moles of calcite dissolved during injection which is written as

$$M_{ca} = \sum_{\Delta t} [Ca]_{out}.Q.\Delta t \quad (3)$$

where $[Ca]_{out}$ (mol/m^3) is the output Ca concentration, Q (m^3/s) is the flow rate and Δt (s) is the sampling interval.

3. Reactive transport modeling of the percolation experiments

3.1. Description of the reactive transport code

The percolation experiments are simulated using the CrunchFlow code (Steefel et al., 2015; Steefel and Molins, 2016), a software package for multicomponent multidimensional reactive transport in porous media. CrunchFlow numerically solves the mass balance for each component while accounting for advection, dispersion and diffusion using an integrated finite difference method. The governing partial differential equation writes as (Steefel et al., 2015)

$$\frac{\partial (\phi C_j)}{\partial t} = \nabla.\left(D\nabla C_j\right) - \nabla\left(qC_j\right) + R_j \qquad \text{(j = 1, 2, 3, …, n)} \tag{4}$$

where ϕ is porosity, C_j is the concentration of component j (mol/m^3), q is the Darcy velocity (m^3/m^2/s), R_j is the total reaction rate affecting component j (mol/m^{3}rock/s) and D is the combined diffusion-dispersion coefficient (m^2/s). The total reaction rate is written as

$$R_j = -\sum_m \nu_{jm} R_m \tag{5}$$

where R_m is the reaction rate (Rm < 0 dissolution, and Rm > 0 precipitation) of mineral m (mol/m^{3}rock/s), and ν_{jm} is the number of moles of component j in mineral m.

Mineral reactions are described using kinetic rate laws. Initial mineral surface area and several reaction rate parameters have to be fed into the code as inputs. For these simulations, the reaction rate laws used are in the form of

$$R_m = -A_m \sum_{terms} k_m \left(\prod_i a_i^{n_i}\right) f_m(\Delta G) \tag{6}$$

where A_m is the mineral surface area (m^2 mineral/m^3 rock), and $a_i^{n_i}$ is the term describing the effect of species i (e.g., H^+, denoting the effect of pH) on the rate. The summation term shows that several parallel rate laws may be used to describe the rate dependence on the pH or other species.

232 k_m is the reaction rate constant (mol/m^{2}mineral/s) at the temperature of interest, i.e., T = 60 ºC
233 (333.15 K) and is calculated from the measured rate constant value at standard temperature (k_{25},
234 see Table A1 for the utilized values) using the Arrhenius law

235 $$ln\left(\frac{k_m}{k_{25}}\right) = -\frac{E_a}{R}\left(\frac{1}{T} - \frac{1}{298.15}\right) \quad (7)$$

236 where E_a (kcal/mol) and R are the activation energy and ideal gas constant, respectively.

237 The $f_m(\Delta G)$ function in Eq. (6) is written as

238 $$f_m(\Delta G) = \left(1 - \left(IAP/K_{eq}\right)^{m_2}\right)^{m_1} \quad (8)$$

239 where ΔG is the Gibbs energy of reaction (J/mol), the term IAP stands for the solution ionic activity
240 product, K_{eq} is the equilibrium constant for the dissolution reaction, and m_1 and m_2 are empirical
241 exponents. The equilibrium constant is temperature- and pressure-dependent (Brantley et al.,
242 2008). Thus, values at representative experimental conditions are used (Table A1).

243 The code solves for the flow field, concentrations of aqueous species, and changes in mineral
244 volume fractions in all grid cells of the numerical domain. The stoichiometric coefficients and log
245 K_{eq} values for the different homogeneous (speciation) reactions are taken from the EQ3/6 database
246 (Wolery et al., 1990; included in the CrunchFlow code) and are listed in Table S1 in Supporting
247 Information. Values of log K_{eq} for the calcite dissolution reaction are taken from the Phreeqc
248 database (v.3.6.2) (Parkhurst and Appelo, 2013), to be able to account for the effect of pressure
249 (included through the changes in the molar volumes of the different species). Activity coefficients
250 are calculated using the extended Debye Hückel formulation (b-dot model) with parameters
251 obtained from the EQ3/6 database included in CrunchFlow. The calculated changes in mineral
252 volume fraction resulting from mineral dissolution/precipitation are used to update the porosity

field at the end of each numerical time step. Appropriate relations are used to update the permeabilities and mineral surface areas following porosity changes (see section 3.5 for further details), which in turn affect the flow and reactive transport processes.

3.2. Model setup

The two cores (25 mm in diameter and 44 or 78 mm in length) are considered as cylinders surrounded by a non-reactive substance, i.e., pure calcite with small porosity (5.8 %), negligible permeability (10^{-22} m^2) and zero surface area (inert), to facilitate simulations and in a 3D square-prism domain. The rock domain is discretized into 20 × 20 × 20 grid cells (1.25 × 1.25 × 2.2 mm^3 each) for the experiment *L_1-CO_2-28* and into 20 × 20 × 22 grid cells (1.25 × 1.25 × 3.54 mm^3 each) for the experiment *L_2-HCl-28* (Fig. 2). To ensure a uniform distribution of fluid flow at the core inlet, a fictitious inlet slice of 20 × 20 grid cells is used. This slice is assumed to be composed of pure calcite with a porosity equal to the average porosity of the sample, very large permeability (10^{-9} m^2), and zero surface area (inert). As a result, the model domains of the *L_1-CO_2-28* and *L_2-HCl-28* experiments consist of a total number of 8400 and 9200 cells, respectively. Details on grids are provided in Table A2.

The initial and boundary conditions used in the model replicate the experimental ones with (1) no-flow lateral boundaries, (2) constant flow rate at the inlet, and (3) constant pressure at the outlet (Fig. 2). The initial pressure in the whole domain is set to 100 and 1 bar for *L_1-CO_2-28* and *L_2-HCl-28* experiments, respectively. Solute transport involves advection, diffusion and dispersion, with a uniform diffusion coefficient of 10^{-9} m^2 s^{-1} for all species in the bulk water, i.e., the typical value for the diffusion coefficient of a component in liquids (Tewes and Boury, 2005; Omrani et al., 2022). Longitudinal and transverse dispersivity are respectively 2.5 × 10^{-3} m, i.e., 0.1 length

scale as a rule of thumb (Reimus et al., 2003) and 2.5×10^{-4} m, i.e., 0.1 of the longitudinal dispersivity (Smith and Chapman, 1983; Park and Lee, 2021).

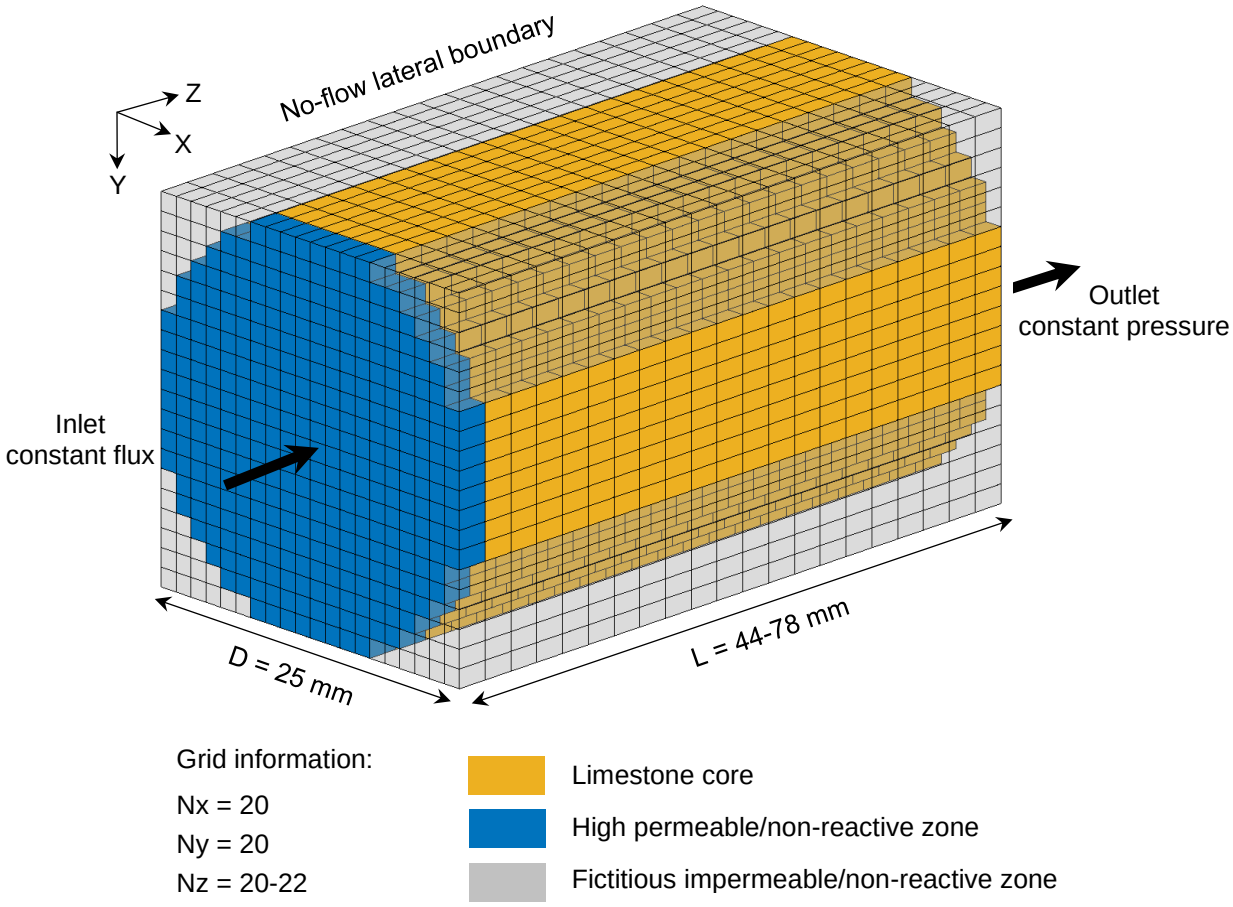

Fig. 2. 3D conceptual model, numerical discretization, and boundary conditions of flow domain used in the reactive transport simulations.

3.3. Rock and solution compositions

The initial volume fraction of calcite in each core, i.e., $1 - \phi_b$, and equilibrium and kinetic rate parameters for calcite (Palandri and Kharaka, 2004; Xu et al. 2012) are listed in Table A1. Equilibrium constants and stoichiometric coefficients for calcite dissolution reaction are taken from the PhreeqC code (v3.6.2) and the PhreeqC database (Parkhurst and Appelo, 2013) for the

experimental pressure and temperature conditions. Initial compositions, i.e., aqueous species and the pH of injecting solutions are also listed in Table A1. The initial pore fluids in both experiments are assumed to be at equilibrium with the calcite at the respective experimental pressure and temperature.

3.4. Digital rock models

Micro-CT images with voxel resolutions of 20 μm and 21 μm for dry L_1 and L_2 cores, respectively, are used to deal with the pore space heterogeneity in the continuum model (see Vafaie et al., 2024 for detials). Arithmetically averaged μCT data on the model grid cells are used to extract effective Darcy-scale porosity maps (initial porosity map in Fig. 1). The image processing workflow is explained in Supporting Information and in Vafaie et al. (2022).

The initial permeability maps of the cores are built by applying an explicit power-law permeability-porosity relationship with an exponent of 3 (initial permeability in Fig. 1; see Section 3.5 for details). The permeability histogram for sample L_1 yields a mean value of 4.7×10^{-14} m^2 with a standard deviation of 1.27×10^{-13} m^2 (Fig. 3). Validity of the initial permeability maps is assessed by using the maps to simulate a water percolation experiment conducted on sample L_1 prior to CO_2-saturated water injection. In this test, water is injected into the core at a constant flow rate of 0.15 mL/min for 3 hours (≈ 5 pore volumes). The differential pressure ΔP across the core after reaching steady state conditions is 0.1 bar, which equals the resolution of the pressure transducers. By imposing the constant flow rate at the inlet, the simulated ΔP is 0.089 bar across the specimen, which agrees well with the measured ΔP. In addition, using the flow rate and numerically measured ΔP in Darcy's law (Eq. 1) returns a bulk rock permeability of 2.55×10^{-14} m^2 consistent with the experimentally measured value of 2.54×10^{-14} m^2 (Table A1). The small absolute relative error of 0.03% in the calculated bulk rock permeability indicates (1) the ability

of the constructed permeability map to effectively reproduce the Darcy-scale single-phase flow behavior of the core under intact conditions and (2) the validity of the described approach to develop the digital rock model. The generated permeability map of sample L_2 yields similar observations.

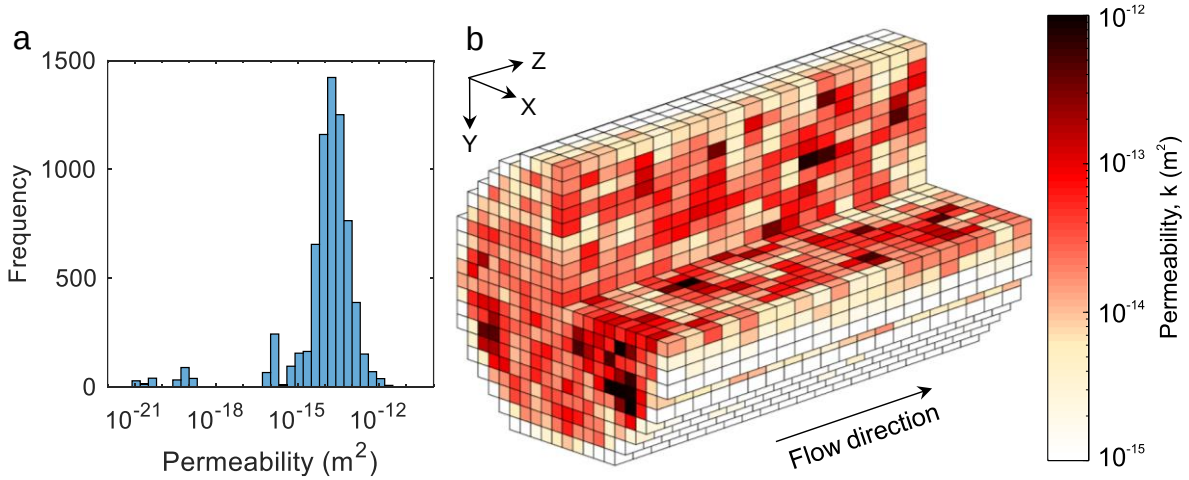

Fig. 3. Permeability map of sample L_1 from Pont Du Gard Limestone: (a) histogram and (b) 3D map of the grid-based distribution of permeability.

3.5. Porosity-permeability-surface area relationship

The porosity-permeability relationship, which couples heterogeneities in pore size distribution and flow field is a critical factor in the modeling of reactive flow at the continuum scale. In this study, a power-law relationship inspired by the original Kozeny-Carman equation (Hommel et al., 2018) is used to calculate the time-dependent variation of the permeability with porosity following mineral dissolution

$$k/k_0 = (\phi/\phi_0)^{n_{grid}} \cdot ((1-\phi_0)/(1-\phi))^2 \quad (9)$$

where ϕ and k are porosity and permeability for each grid cell, respectively, and ϕ_0 and k_0 are reference porosity and permeability values. The exponent n_{grid} is an empirical parameter. By setting n_{grid} = 3, the equation returns the original form of the Kozeny-Carman equation for permeability calculations in numerical grids, which is assumed to apply to our intact samples and is used to build the initial permeability maps. During the initialization stage, ϕ_0 and k_0 respectively refer to the experimentally measured bulk porosity and permeability of the cores. During the reactive flow stage, the exponent n_{grid} may deviate from the initial value. Different n_{grid} values are used to reproduce the experimental observations (Fig. 1). In this stage, ϕ_0 corresponds to the bulk porosity of the core and k_0 equals the initial permeability value in each grid cell. Accordingly, heterogeneity only appears in the permeability map. Figure 4 shows the full range of permeabilities in the grid cells and their evolution with porosity changes for sample L_1. The same trend also applies to sample L_2.

CrunchFlow uses two distinct simple relations to calculate changes in mineral surface area A_m (m^2_{min} m^{-3}_{bulk}), proportional to porosity variation owing to mineral dissolution and precipitation

$$A_m = A_{m_0}(\phi/\phi_0)^{2/3}((1-\phi)/(1-\phi_0))^{2/3} \quad \text{mineral dissolution} \quad (10)$$

$$A_m = A_{m_0}(\phi/\phi_0)^{2/3} \quad \text{mineral precipitation} \quad (11)$$

where A_m is the mineral surface area in each grid cell varying with the corresponding cell porosity and A_{m_0} is the initial value for this parameter. Since calcite is the only mineral in this particular system, $1-\phi$ represents the mineral volume fraction. It is worth noting that mineral dissolution is the only reaction in the conducted experiments.

Several approaches can be employed to adjust the initial reactive surface area in contact with the fluid per unit volume of rock (A_{m_0}) using information on either grains or pore geometry (Brosse

et al., 2005; Lai et al., 2015; Al-Khulaifi et al., 2017; Garcia-Rios et al., 2017) or using phenomenological or empirical laws (Noiriel et al., 2009). In our study, however, the initial surface area is treated as a fitting parameter. We change the A_{m_0} with n_{grid} = 3 to match the effluent Ca concentration during the first 1-2 days of injection. It is assumed that at this stage, the short advance of the dissolution front can not affect the localization of flow and hence the selected n_{grid} value. As a result, we obtain A_{m_0} = 59 m^2_{min} m^{-3}_{bulk} and A_{m_0} = 55 m^2_{min} m^{-3}_{bulk} for the CO_2 and HCl experiments, respectively. These values are within the (wide) range of values measured for the reactive surface area of calcite in the literature (Noiriel et al., 2009; Luo et al., 2012; Beckingham et al., 2016; Garcia-Rios et al., 2017; Cama et al., 2019). The reactive surface area in contact with the fluid in each grid cell could theoretically follow two general trends: (1) decreasing as a result of mineral precipitation although it is not relevant to our case dominated by mineral dissolution reactions or (2) initially increasing, reaching a maximum peak, and then declining owing to the dissolution-induced porosity enhancement (see the example for sample L_1 in Fig. 4). As the surface area approaches zero for the two extreme scenarios of ϕ = 0 and ϕ = 1, Eq. (10) and (11) ensure that no further precipitation or dissolution can take place, respectively.

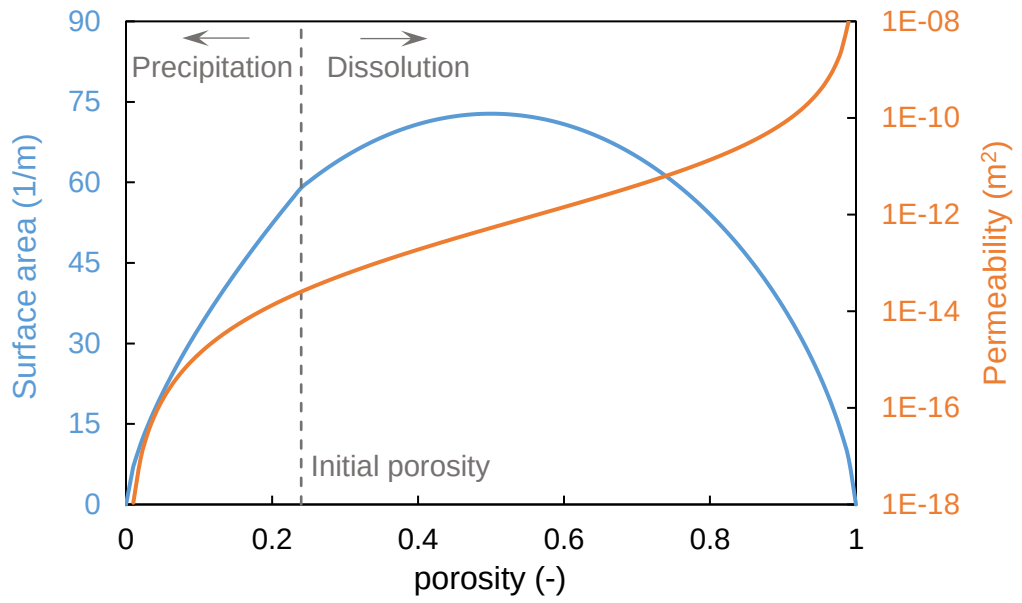

Fig. 4. Possible range of changes in the reactive surface area and permeability (using n = 3 in Eq. 9) for each numerical grid cell as a result of chemically-induced changes in porosity for sample *L1*. Precipitation (decrease in porosity) does not apply to these experiments.

4. Results

4.1. CO_2-saturated water injection: wormhole formation

4.1.1. Experimental results

Figure 5a shows the variation in the output Ca concentration ($[Ca]_{out}$) as a function of time in the CO_2-saturated water injection experiment (*L1-CO2-28*). $[Ca]_{out}$ is always higher than zero throughout the experimental run, indicating a continuous calcite dissolution (discrete points in Fig. 5a). In this experiment Ca is released in three different stages defined by (1) an initial peak of $[Ca]_{out}$ related to the propagation of dissolution front along the core length, followed by (2) a substantial drop in $[Ca]_{out}$ possibly due to the localization of flow in preferential flow pathways causing a decrease in the accessible reactive surface area with time, and (3) a steady-state $[Ca]_{out}$

as a result of complete localization of flow and reaction yielding a constant accessible reactive surface area. The small increase in the $[Ca]_{out}$ between the second and the fourth days is caused by our attempts to find an appropriate injection rate, i.e., the maximum possible injection rate, at the beginning of the experiments and it should not be taken as part of the evolution of the dissolution pattern.

Calcite dissolution results in porosity enhancement in sample L_1. The porosity enhancement obtained from solution chemistry analysis ($\Delta\phi_{[Ca]out}$) is 5.5% and 9.31% after 14 and 28 days of injection, respectively, which agrees well with values obtained from weight measurement ($\Delta\phi_{bulk}$) (Table 1). The total enhancement in μCT porosity of sample L_1 ($\Delta\phi_{\mu CT}$) is 4% and 13.8% after 14 and 28 days of injection, respectively, showing non-negligible differences with those measured by the other methods (Table 1). The imaging method underestimates the initial porosity of the cores as pores with sizes smaller than the μCT resolution remain unrecognized. As the dissolution process enlarges sub-resolution pores and/or creates connections between them, making them detectable by the CT, the inferred porosity enhancement may be overestimated.

Table 1 Experimental conditions, porosity, and permeability of intact and altered cores. The asterisk (*) denotes measurement after 14 days. Q = 0.15 mL min^{-1} for both experiments. ϕ_{bulk}: porosity calculated by weight measurement. ϕ_{CT}: porosity calculated by µCT imaging data. $\Delta\phi_{bulk}$: porosity changes based on weight measurements. $\Delta\phi_{CT}$: porosity changes based on µCT imaging data. $\Delta\phi_{ICP}$: porosity changes based on effluent chemistry analyses.

experiment	**experimental conditions**		**state** intact/altered	**ϕ** [%]		**Δϕ** [%]			**permeability**
	PCO₂ (bar)	***T*** (°C)		**bulk**	**µCT**	**bulk**	**ICP**	**µCT**	k (m^2)
L₁-CO₂-28	100	60	intact	23.8	9.5				2.54×10^{-14}
			altered*	29.7		5.9	5.5	4.0	3.64×10^{-11}
			altered	33.5		9.67	9.31	13.78	5.51×10^{-11}
L₂-HCl-28	4×10^{-4}	60	intact	28.5	8.0				3.76×10^{-14}
			altered	29.4		0.9	0.8	1.7	2.69×10^{-13}

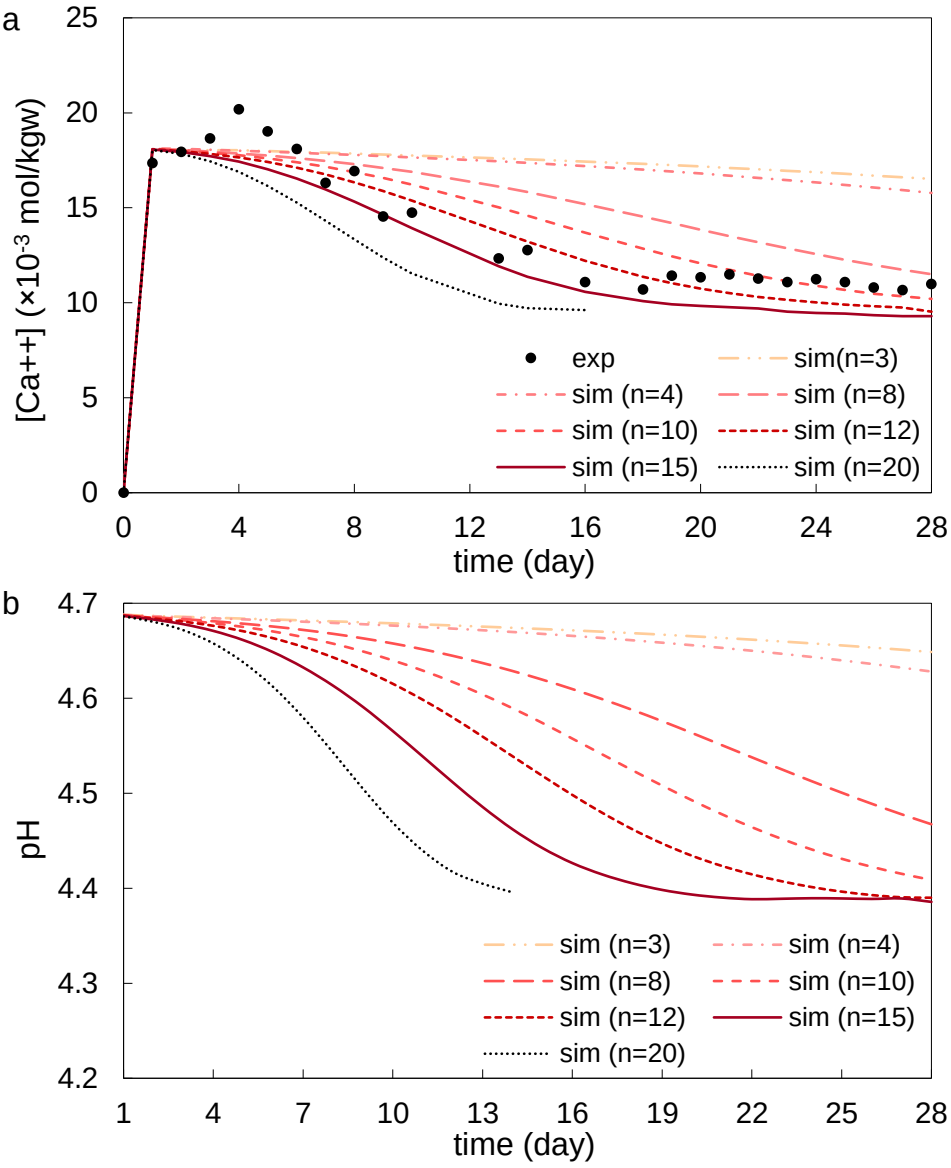

404

405

406 **Fig. 5**. Experimental and simulated variation in the output fluid chemistry over time in the L_1

407 experiment with n_{grid} = 3, 4, 8, 10, 15, and 20 (Eq. 9): (a) Ca concentration and (b) solution pH.

408 Line colors are gradually lightened with the decrease in the n_{grid} value. Note that the analytical

409 uncertainty in experimental Ca concentration is around 3%.

410

411 A comparison between CT images of the sample before and after injection with CO_2-rich water

412 accredit the dissolution pattern inferred from the effluent chemistry analysis (Fig. 6). We observe

that calcite dissolution leads to porosity enhancement, albeit not uniformly, along the L_1 core. The increase in porosity is larger near the inlet (first 5 mm) with an average increase of 57.5% after 28 days. A smaller increase in average porosity (5.2%) occurs over the remaining length of the core overall forming a conical wormhole shape (Fig. 7c). Wormhole formation roughly parallel to the flow direction accounts for the decreasing trend and the subsequent steady release of $[Ca]_{out}$ after the initial peak in the $[Ca]_{out}$ profile (Fig. 5a). As calcite dissolves and the wormhole propagates through the core, the localization of flow in the wormhole restricts the fluid-rock interactions to this channel, reducing the effective accessible reactive surface area and calcite dissolution. When the wormhole reaches the core outlet, the flow and, hence, calcite dissolution, are limited solely to the wormhole wall, yielding a constant $[Ca]_{out}$ release. The porosity enhancement in the form of a wormhole also results in a substantial increase in the permeability of the sample by 3 orders of magnitude (Table 1).

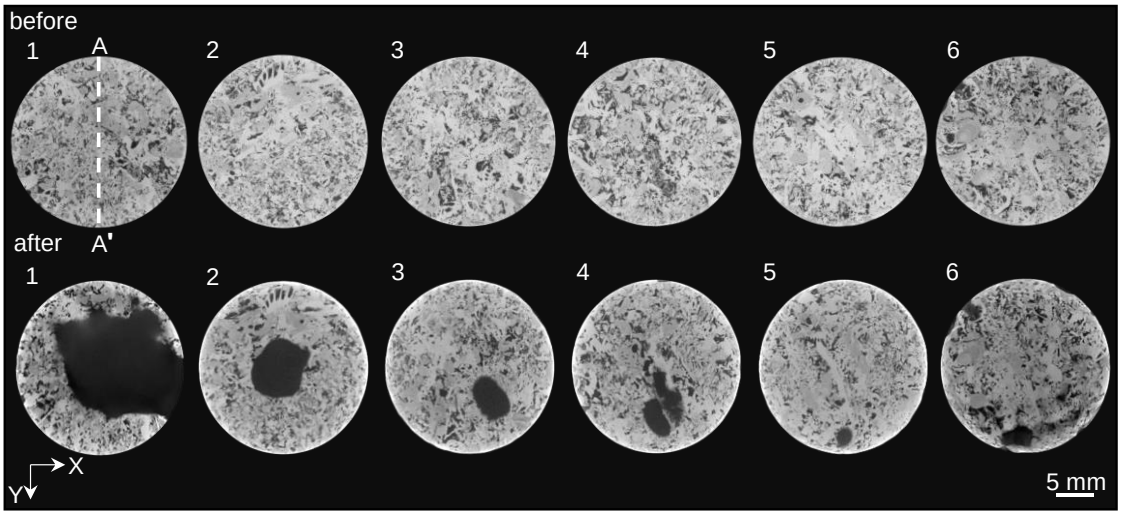

Fig. 6. 2D gray-scale µCT cross-section images perpendicular to the flow direction (Z) along the L_1 core before (upper row) and after (lower row) 28 days of reaction with CO_2-saturated water. In the lower sequence, the dark area is new porosity caused by calcite dissolution. The numbers

indicate the position of the images along the Z axis separated by a constant distance of 0.88 mm (1: inlet, 6: outlet). Section AA´ along the core is used in Figs. 7 and 8.

4.1.2. Numerical simulations

Simulation results show that fluid flow and calcite dissolution begin to concentrate in areas of high porosity and high permeability from the onset of the experiment (Fig. 8). A comparison between the μCT cross-section image of the core inlet before CO_2 injection (Fig. 6) and the respective simulation result (Fig. 8) shows that calcite dissolves at the same locations over short periods (≈ 96 h) irrespective of the n_{grid} value used.

As the dissolution front penetrates further into the core and is localized in the heterogeneous pore structure of the limestone, the exponent n_{grid} starts to play a critical role in the evolution of fluid flow and chemistry. Variation of $[Ca]_{out}$ and μCT porosity profiles are used as useful criteria to understand the effect of n_{grid} on the temporal and spatial development of dissolution in the limestone. Increasing n_{grid} lowers $[Ca]_{out}$ because of the gradual localization of dissolution in preferential flow pathways (Fig. 5a). While the estimated outflow concentration profiles drop steadily with $n_{grid} < 8$, the change in the slope of the curves representing wormhole breakthrough across the core can only be captured when larger n_{grid} values are used. This change is slight and occurs after ≈ 24 days for $n_{grid} = 10$ but becomes sharper and occurs earlier for $n_{grid} = 12$ and 15. An optimal match with experimental results is achieved with $n_{grid} = 15$ for which the absolute relative error for measured $[Ca]_{out}$ varies between 4% to 15%. Larger n_{grid} values result in unrealistically fast localization of flow and underestimation of calcite dissolution by up to 45%.

Simulations show that calcite dissolution takes place mainly near the injection point with $n_{grid} = 3$, yielding a compact dissolution pattern (Fig. 7 d,j). By increasing n_{grid} to 15, the developed

dissolution pattern gradually evolves toward a major wormhole as observed in μCT images (Fig. 7 c,o). For n_{grid} = 15, the simulated shape and orientation of the dissolution front match well the observed dissolution pattern (Fig. 7c). The wormhole deviates toward the right on the Y axis, i.e., through a region of high initial porosity (Fig. 7a). Moreover, simulation results show the formation of a localized dissolution zone simultaneously but in opposite direction to the main wormhole where a less pronounced initially high porosity zone exists. Nevertheless, the calculated porosity does not perfectly conform to μCT estimates, particularly in the wormhole area ($\phi_{CT}\approx1$). Accordingly, the model predicts a total porosity enhancement of 6.2%, which is slightly smaller than direct measurements (9.7%, Table 1).

Porosity reaches values higher than 70% only in a limited number of cells (i.e., 41 cells out of the total 8,400 cells of the numerical domain) near the core inlet. In these cells, permeability could reach very high values considering the utilized n_{grid} =15 in Eq. (9). These values, although overestimating the permeability in these grid cells, are still within the same order as those estimated for a planar fracture of the same aperture by the cubic law or a tube of the same diameter using the Poiseuille–Hagenbach equation (Sahimi, 2011). Nevertheless, as the number of these cells is very limited, the overestimation of permeability in these cells is not critical and the utilized power-law porosity-permeability relationship (Eq. 9) can satisfactorily reproduce the experimental observations.

Although outflow pH is not measured in the CO_2-saturated water experiments, simulation results provide insights into pH evolution at the core outlet (Fig. 5b). Output pH is 1.55 units higher than that of the input solution pH (3.13) after one day of injection as a result of proton consumption during calcite dissolution. The increase in pH diminishes during the experiment and also with the increase in n_{grid} (Eq. 10) where the formation of a channel-like dissolution pattern forces most of

the injected fluid to move through the high permeability channel without reacting with the remaining part of the limestone, maintaining the solution acidity. Consequently, although the fluid pH increases slightly while passing through the limestone core, it remains acidic and undersaturated with respect to calcite during the experiment.

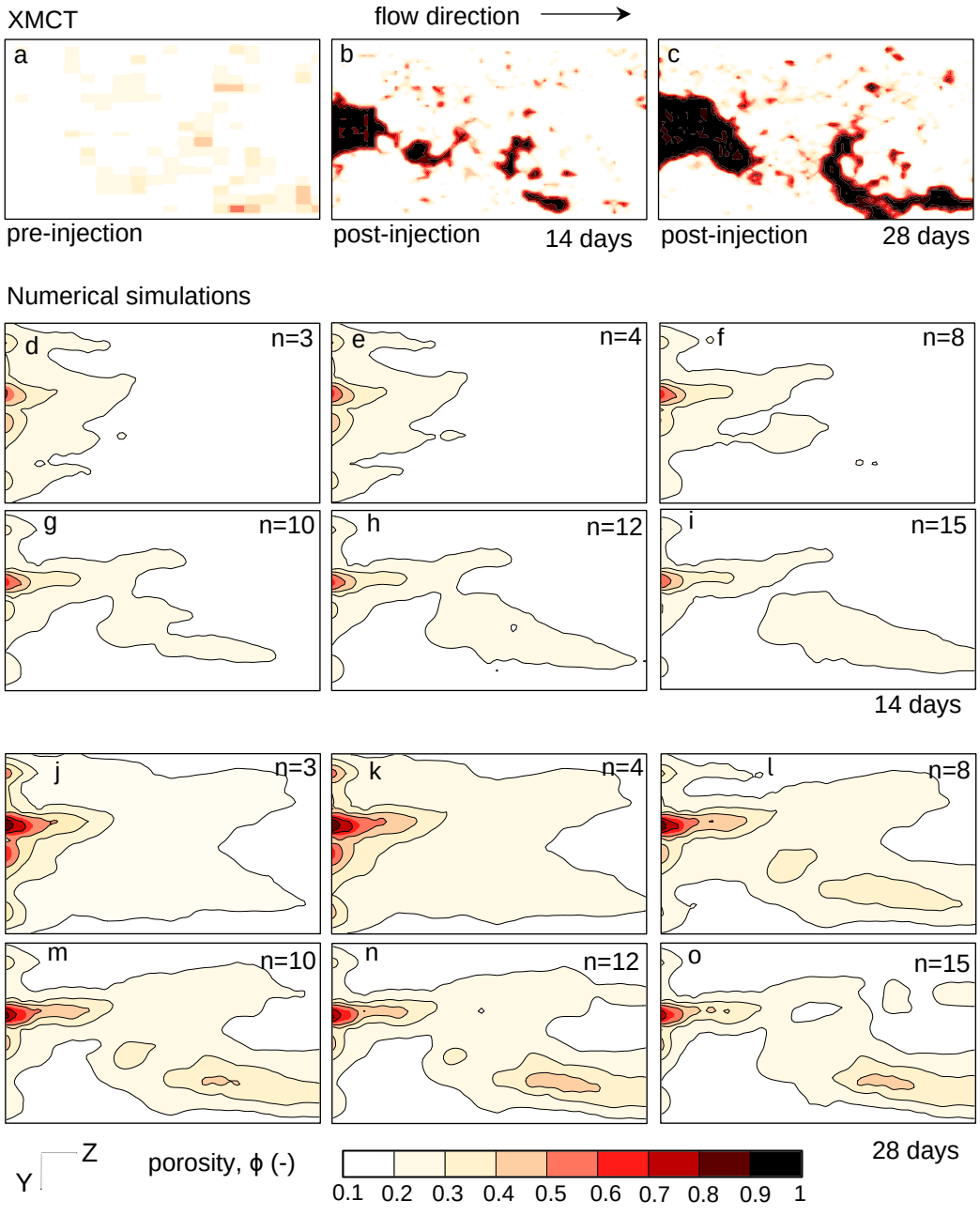

Fig. 7. Experimental (a-c) and simulated (d-o) distribution of porosity in a cross-section along the flow direction in sample L_1 (section AA' shown in Fig. 6): (a) before CO_2 injection and (b,c) after CO_2 injection for 14 days and 28 days inferred from µCT images; (d-o) simulations after reaction with CO_2-saturated water for 14 days and 28 days using n_{grid} = 3, 4, 8, 10, 12, and 15 (Eq. 9).

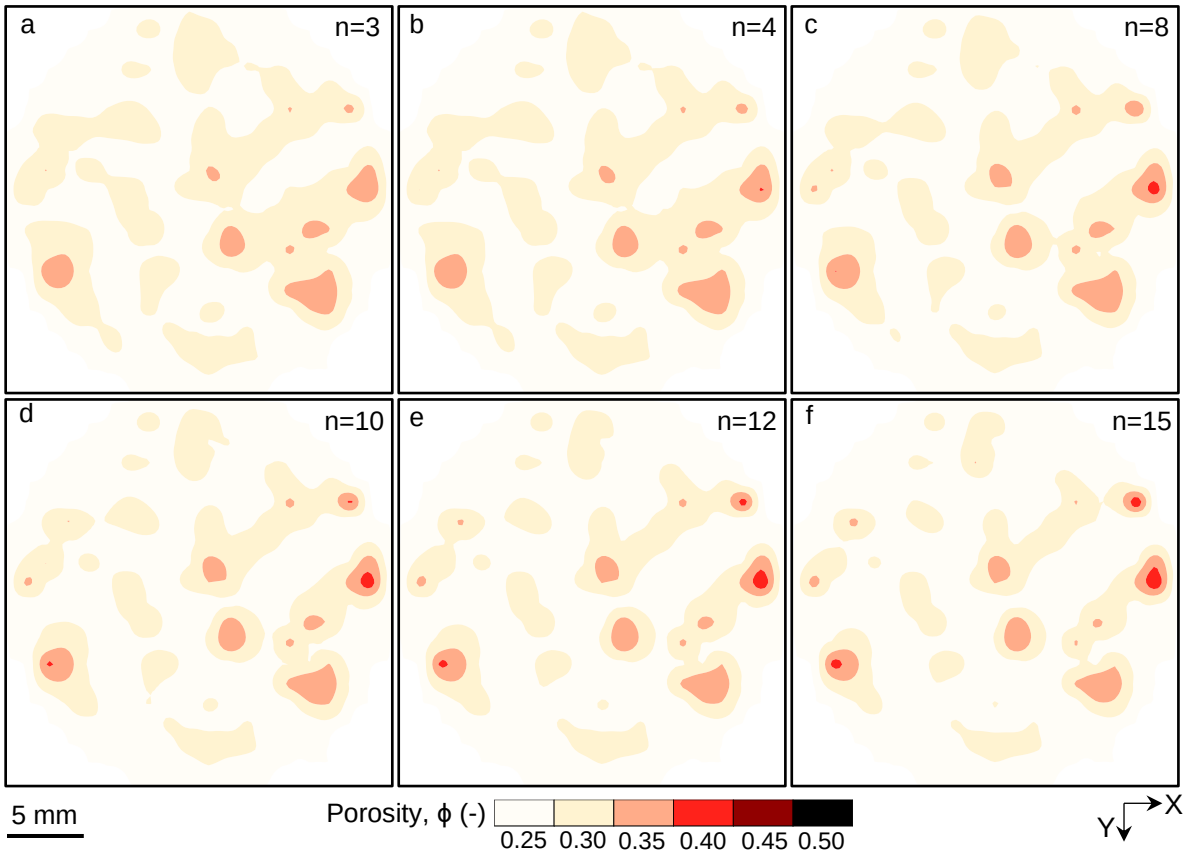

Fig. 8. Simulated spatial development of porosity at the core inlet after CO_2-saturated water injection for 96 h using porosity-permeability relationship (Eq. 9) with n_{grid} ranging between 3 and 15 (a-f).

The simulation data is used to estimate the evolution of bulk rock permeability upon reaction with CO_2-rich water (Fig. 9), while direct experimental measurements are made only before and after

14 and 28 days of injection. To this end, the calculated pressure difference across the core at a constant flow rate (0.15 mL/min) is used in Darcy's law (Eq. 1) to calculate the average core permeability. A comparison between the calculated permeability (1.7×10^{-11} m^2) after 28 days with the experimentally measured value (5.5×10^{-11} m^2, Table 1) shows that both are of the same order of magnitude. However, the model permeability at an earlier stage (14 days) is underestimated by a factor of 20 ($k_{model} = 1.8\times10^{-12}$ m^2, $k_{experiment} = 3.6\times10^{-11}$ m^2 (Tabe 1)). This difference may arise from the morphology of the dissolution pattern: a narrow wormhole forms along the core within 14 days yielding a highly permeable path while simulations predict a relatively thicker wormhole structure with a locally smaller increase in porosity (Fig. 7i) yielding larger overpressures at the inlet and equivalently smaller permeability. The porosity-permeability relationship for the full core is fitted with a power law with an exponent (n_{core}) of 27.6 (Eq. 9) which is 1.8 times larger than $n_{grid} = 15$ used at the grid scale.

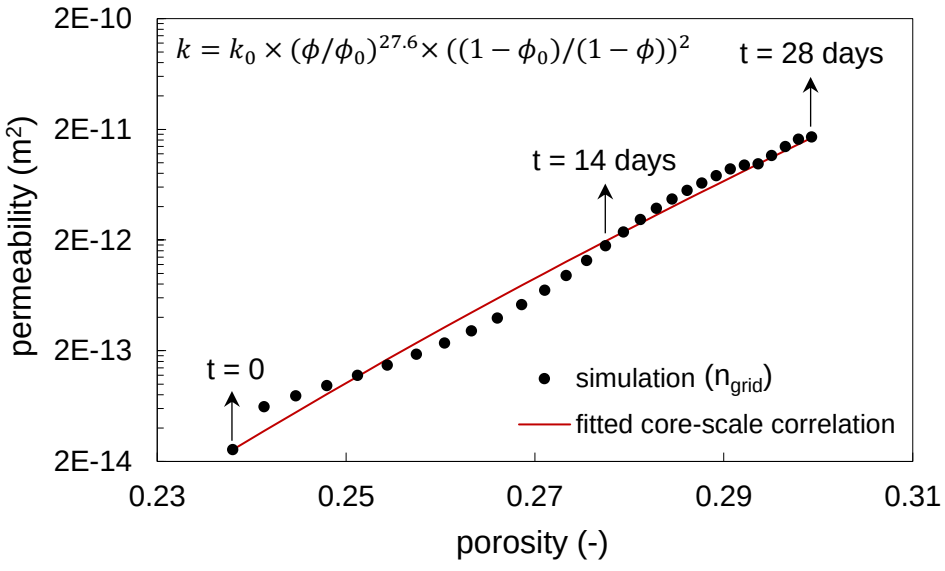

Fig. 9. Change in bulk core permeability as a function of average porosity estimated from numerical simulations (black circles). The fitted core-scale power-law correlation (solid line) corresponds to an exponent n_{core} of 27.6.

4.2. HCl solution injection: compact dissolution

4.2.1. Experimental results

Injection of the HCl solution was performed at the same flow rate as in the CO_2 experiment, i.e., under the same Péclet number (advection to diffusion ratio). Figures 10a and 10b show the variation in the measured $[Ca]_{out}$ and pH in the experiment (*L_2-HCl-28*). Similar to the CO_2 experiment, $[Ca]_{out}$ is larger than zero throughout the experiment demonstrating continuous calcite dissolution. Input pH is the same as that in the CO_2-saturated water experiment in the first 17 days of injection, meaning that the Damköhler number (ratio of reaction rate to advection) would be the same. However, $[Ca]_{out}$ is about 10 to 20 times smaller. The $[Ca]_{out}$ evolution is also different from that in the CO_2 injection experiment implying that the type of the injected acid largely controls the dissolution process in the rock. In the *L_2-HCl-28* experiment, $[Ca]_{out}$ is practically constant during the experimental run. The reduction in pH of the injected solution (pH $\approx$ 2.66) in the second stage of the experiment (last 11 days) yields an increase in $[Ca]_{out}$ by a factor of 3 due to faster calcite dissolution, which remains constant until the end of the experiment. Nevertheless, the overall dissolution rate in this stage is significantly lower than that achieved by CO_2-saturated water.

Slight calcite dissolution in the HCl injection experiment causes an increase in the porosity of sample *L_2* by $\approx$ 1% (Table 1). Comparison between the porosity maps along the core before and

after the experiment shows that calcite dissolves only at the core inlet yielding a compact (face) dissolution pattern (Fig. 11) and a 7-fold increase in permeability.

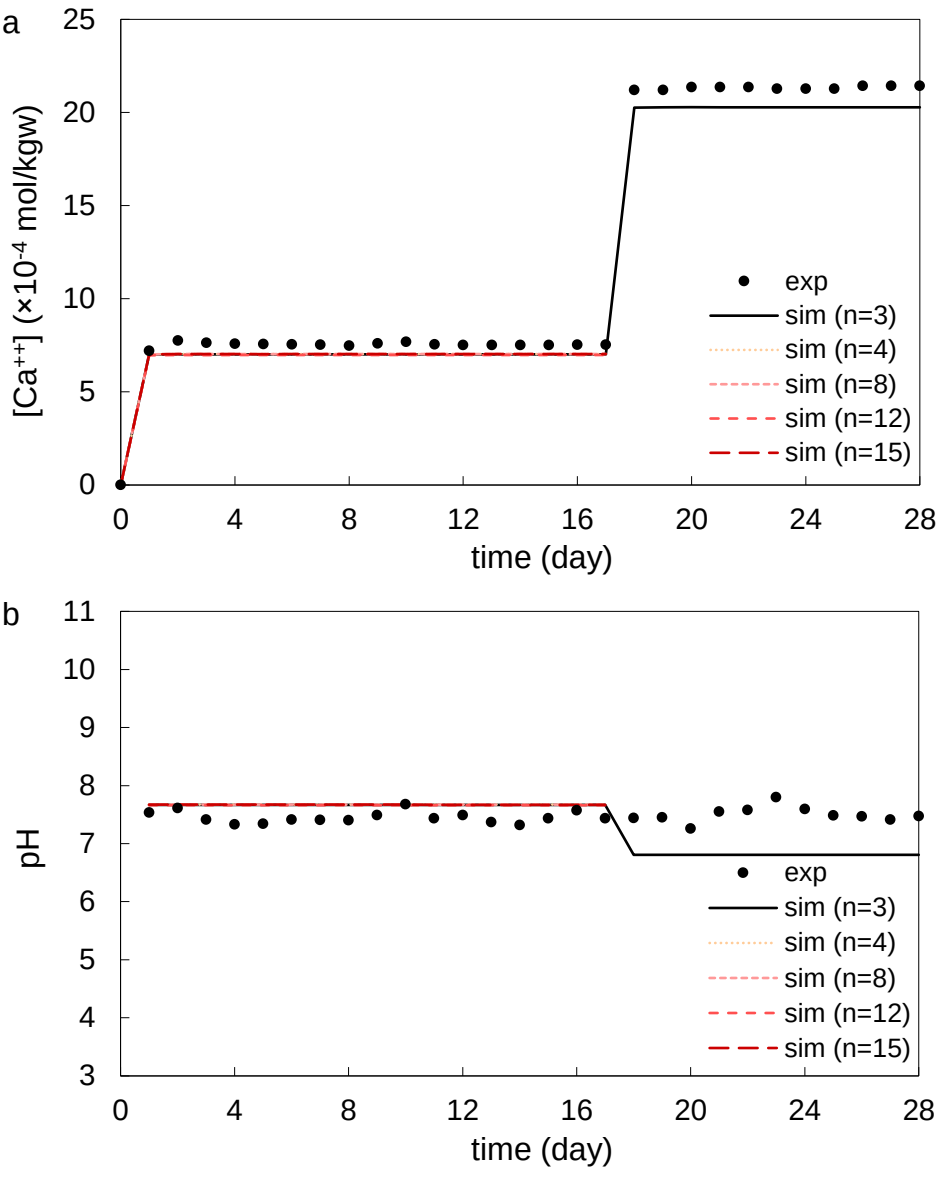

Fig. 10. Experimental (solid symbols) and calculated (lines with n_{grid} = 3, 4, 8, 12, and 15) chemical changes in the experiment *L_2-HCl-28*: (a) output Ca concentration and (b) output pH. Note that $[Ca]_{out}$ is one order of magnitude smaller than in the CO_2-saturated water injection (Fig. 5). Simulation results coincide with each other because the variation of n_{grid} in Eq. (9) does not have

any significant effect at the temporal scale of the experiment. Note that the analytical uncertainty in experimental Ca concentration is around 3%.

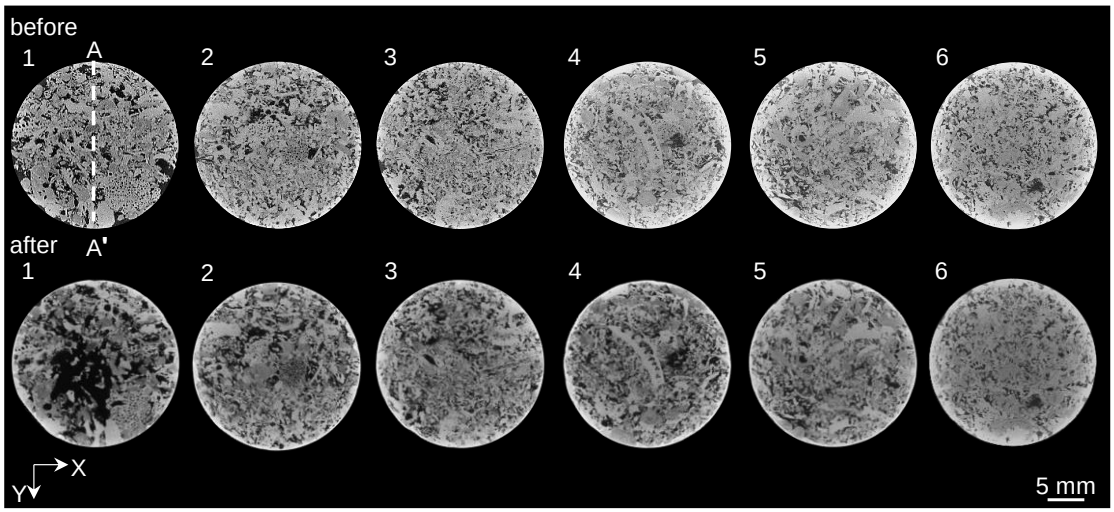

Fig. 11. 2D gray-scale µCT images perpendicular to the flow direction (Z) along the L_2 core before (upper row) and after (lower row) reaction with HCl solution. The large dark area in the first slice after injection shows dissolution-induced porosity enhancement concentrated at the inlet (compact dissolution). The numbers indicate the position of the images along the Z axis separated by a constant distance of 1.56 mm (1: inlet, 6: outlet). Section AA´ along the core is used to plot results in Fig. 12.

4.2.1. Numerical simulations

Figures 10 to 12 compare the measured and simulated $[Ca]_{out}$ and pH variation as well as the dissolution front structure for sample L_2. The steady-state $[Ca]_{out}$ in both injection stages, the variation in effluent pH (Fig. 10) and the observed compact dissolution pattern (Fig. 11) are satisfactorily reproduced using the conventional cubic porosity-permeability relationship (n_{grid} = 3 in Eq. (9); Fig. 12). With n_{grid} = 3, the difference between calculated and measured $[Ca]_{out}$ varies

between 2.6% to 9.5%. Both model and experimental results present a constant outflow pH of ≈ 7, indicating a significant drop in solution acidity after passing through the rock. Indeed, calcite dissolution neutralizes the pH while reaching equilibrium with calcite. Note that the significant pH increase in the HCl experiment compared with the slight one in the CO_2-saturated water experiment (pH increase of only 1.55) is due to the effect of the type of acid on calcite dissolution. It should be noted that for n_{grid} = 3, the error in calculated outflow pH values is always smaller than 10%.

The exponent n_{grid} values higher than 3, including n_{grid} = 4, 8, 12, and 15, are used to simulate the first stage of the injection experiment on sample L_2 (Fig. 10). The change in n_{grid} results in only a slight change in the dissolution front shape and practically no variation in the amount of dissolved calcite. Given the small amount of calcite dissolved, an increase in the n_{grid} value does not improve the match between the model and the porosity distribution. All simulations predicted an increase in bulk porosity of ≈ 0.7%, which agrees well with the experimental measurements.

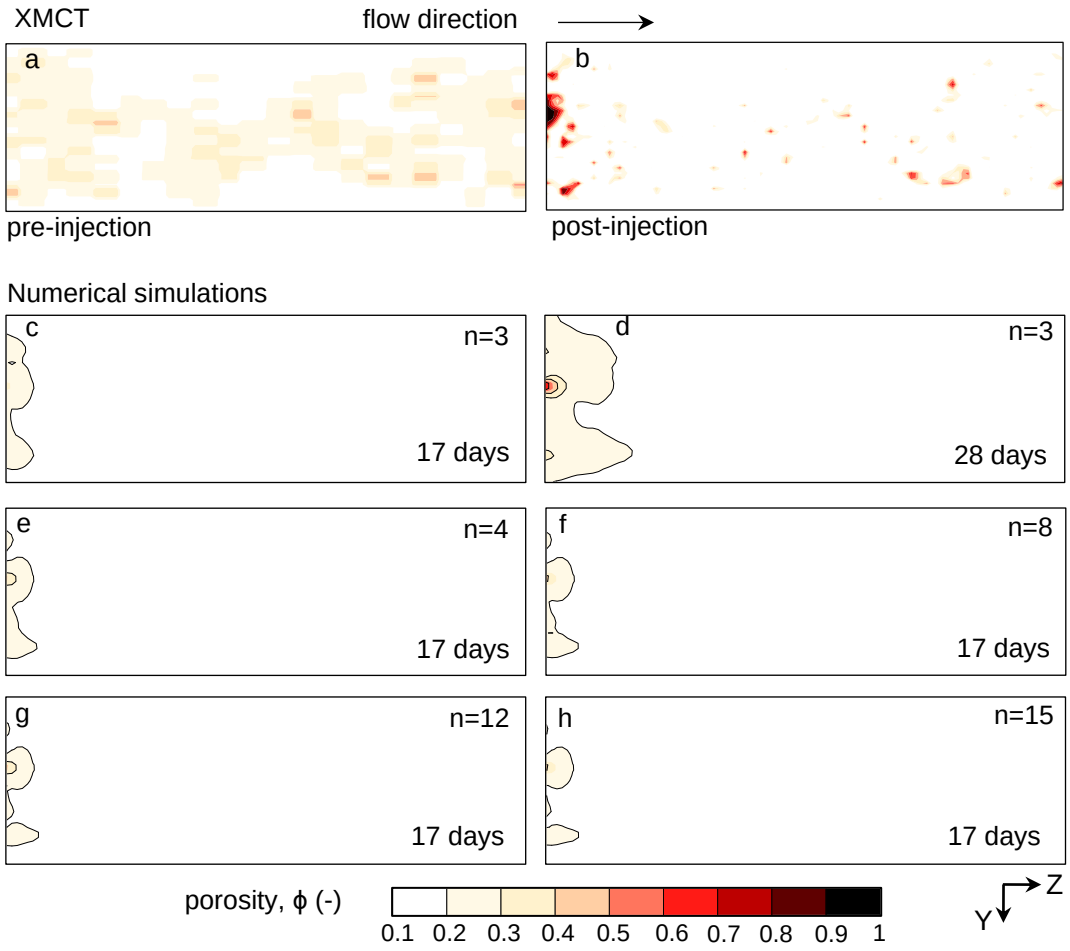

Fig. 12. Distribution of measured (a,b) and simulated (c-h) porosity in a cross-section along the core L_2 (section AA' shown in Fig. 11): (a) before and (b) after HCl injection inferred from µCT images; (c,d) simulations of the core-HCl interaction after17 and 28 days using n_{grid} = 3, and (e-h) simulations of core-HCl interaction after 17 days using n_{grid} = 4, 8, 10, 12 and 15 (Eq. 9).

5. Discussion

5.1. Limitations of the numerical models

The developed 3D Darcy-scale reactive transport model satisfactorily captures the general structure, i.e., shape and orientation, of dissolution patterns formed in the CO_2-saturated water and

HCl experiments. The model is also capable of reproducing the bulk flow and chemical behavior of the cores, including changes in porosity, permeability and dissolved calcite mass in the experiment. It can also qualitatively reproduce the μCT- porosity distribution along the core. Yet, quantitative deviations from laboratory measurements are observed and could arise from three factors.

The main factor is the size of the grid cells in the continuum model selected to afford computational costs. Coarse meshing schemes unavoidably mask some details of the pore space heterogeneity, affecting flow and reaction processes at the grid scale. The second factor could be the representation of the pore structure heterogeneity only in terms of the initial permeability distribution in the rock. Indeed, the initial mineral surface area in the model is treated as a fitting parameter with a uniform distribution over the domain similar to the porosity distribution. The reactive surface area changes with dissolution-induced porosity enhancement (Eq. 10) gradually reaching a heterogeneous distribution as flow and chemical reactions localize in regions of high local permeability. Yet, neglecting initial heterogeneities in the reactive surface area may affect the spatial distribution of chemical reactions while returning reliable predictions at the bulk scale.

The third factor that brings in differences between experimental and simulation results is the surface area-porosity relationship (Eqs. (10) and (11)). Since this correlation is developed based on a simple representation of porous media, i.e., a package of spherical or regularly-shaped grains of the same size (Noiriel et al., 2009), the effects of grain geometry and grain size distribution on the evolution of the mineral surface area are overlooked (Noiriel et al., 2009; Soulaine et al., 2018). Noiriel et al. (2009) showed that neglecting realistic grain shapes by Eqs. (10) and (11) could result in erroneous estimates of the reaction rate. Imaging techniques such as X-ray tomography could be useful to have more realistic estimates of mineral surface area while considering the geometry

of grains and their size distribution (Noiriel et al., 2009; Lai et al., 2015; Ling et al., 2022). However, the applicability of the estimated surface area values in reactive transport models is limited, since these estimates strongly depend on the scale at which the process is observed, i.e., the image resolution (Qin and Beckingham, 2021). Yet, employing more complex models that involve adequate physics of the evolving mineral surface area could improve the simulations if they do not contain additional fitting parameters (Gautier et al., 2001; Lüttge et al., 2003; Noiriel et al., 2009).

5.2. Role of pore space heterogeneity and acid type on the development of dissolution

Experimental and simulation results consistently indicate the importance of pore space heterogeneity on the initiation and development of heterogeneous dissolution patterns. The insights gained from numerical simulations show that the acidic fluid largely moves through the preferential flow pathways of higher permeability from the onset of injection and dissolves calcite in the adjacent regions (Figs. 7 and 8). Localization of flow and hence dissolution reactions eventually lead to heterogeneous dissolution patterns. This observation is consistent with earlier studies that commonly show non-homogeneous dissolution regimes in inherently heterogeneous carbonate rocks (Luquot and Gouze, 2009; Ott and Oedai, 2015; Menke et al., 2016; Al-Khulaifi et al., 2017; Dávila et al., 2020). Furthermore, our simulations underscore the tight coupling of fluid flow and chemical reactions in reactive rocks as (1) a simple model considering initial heterogeneity only in terms of permeability field is capable of capturing observed experimental trends, and (2) the porosity-permeability relationship plays a critical role in model performance.

Intrinsic heterogeneities, however, can not completely justify different dissolution regimes (compare Figs. 7 and 12) and rates (compare Figs. 5 and 10) observed in two experiments with the

same limestone and acidic solutions of the same pH using the same flow rate (i.e., identical Péclet and Damköhler numbers). The type of acidic solution is the primary variable that drives these differences and should be considered when assessing acid-rock interactions. Dissolved CO_2 (carbonic acid) is a weak acid, which dissociates only partially (Dávila et al., 2017; Garcia-Rios, 2015) and provides a low-pH solution all along the core. The feedback between flow and long-lasting chemical reactions forms a deep penetrating dissolution front in the core, eventually creating a wormhole (Fig. 6, Fig. 7c). By contrast, the HCl solution acts as a strong acid completely dissociating into its ions (Bernadiner et al., 1992; Raj and Pal, 2014; Dávila et al., 2017; Liu et al., 2022), not buffering the pH and resulting in strong calcite dissolution at the core inlet and fast equilibration and pH increase to ≈ 7 (Fig. 10). pH neutrality hinders further advancement of the dissolution front through the core and yields a compact dissolution pattern (Fig. 11).

Dimensionless Péclet (*Pe*) and Damköhler (*Da*) numbers, respectively defined as the ratio of advective to diffusive transport rates and the ratio of the overall dissolution to the advective transport rates, are commonly used to characterize the dissolution regimes in carbonate rocks (Golfier et al., 2002; Menke et al., 2017; Oelkers, 2018). Our experiments are dominated by advection and are characterized by a *Pe* larger than 1, while the *Da* number is below 10^{-3} (see Vafaie et al., 2023b for calculation details), which should theoretically result in a uniform dissolution regime (Golfier et al., 2002; Luquot and Gouze, 2009; Ott and Oedai, 2015). This prediction, however, deviates from the wormholing (Fig. 6) and compact dissolution (Fig. 11) regimes caused by CO_2 and HCl injections, respectively. Our observations indicate that these numbers are not sufficient to describe the formation and evolution of dissolution patterns in carbonate rocks as they overlook the effects of intrinsic rock heterogeneity and acid type.

5.3. Porosity-permeability relationships

We have used simple power-law relationships between porosity and permeability to study the coupling of flow and reaction in carbonate rocks using Darcy-scale models. More complex models incorporating detailed structural and physical features of porous media can be used instead to reproduce the results. Yet, the application of such models in large-scale simulations may become limited by the need for more information about the pore structure of the rock and the computational costs of their implementation (Hommel et al., 2018).

Simulation results show that the classical power-law porosity-permeability relationship with n_{grid} = 3 (Eq. 9) can only satisfactorily reproduce the compact dissolution in the HCl-limestone system, given the small porosity changes in the time scale of the experiment. An exponent n_{grid} = 3 limits the increase in permeability for a given porosity change and distributes the acidic solution more evenly across the core cross-sections. As a result, mineral dissolution intensifies near the core inlet, leading to a slower propagation of the dissolution front. In contrast, dissolution features in the CO_2-treated specimen can only be reproduced using a high n_{grid} value (n_{grid} =15). A higher n_{grid} value indicates a greater sensitivity of permeability to porosity changes and assists acidic fluid channeling into the cores.

Permeability changes in chemically altered carbonate rocks could be much larger than what is predicted by the classical Kozeny-Carman equation (n_{grid} = 3, Eq. 9). Consequently, permeability increase in such rocks is not exclusively correlated with the change in bulk porosity and depends strongly on the type of dissolution patterns (Fig. 9). The analysis presented here highlights a marked change in the porosity-permeability relationship with n_{grid} = 15 and n_{core} = 27.5 respectively for the mm-scale numerical grids and the cm-scale core. The obtained exponent representing the bulk core flow evolution is consistent with fitted values for bulk porosity and

permeability in earlier experimental studies (Noiriel et al., 2005; Hao et al., 2013; Garing et al., 2015; Smith et al., 2017; Menke et al., 2016 and 2017; Voltolini and Ajo-franklin, 2019; Hao et al., 2019). These observations point to strong scale dependence of porosity-permeability relationships and uncertainties in estimating permeability changes in chemically altering carbonate rocks as heterogeneities tend to grow across scales.

Analysis of field-scale reactive flow will still be challenging with calibrated models for cm-long core samples since corresponding REVs of field injections are usually large (several-meter size) (Cavanagh and Ringrose, 2011). Developing a rigorous upscaling approach could benefit from intermediate-size experiments in underground rock laboratories (Tangirala et al., 2024, Ziegler et al., 2024). Reactive transport simulations of these experiments could employ calibrated core-length parameters to parameterize meter-to-decameter-scale models following the approach used in this study. In this way, multi-step implementation of Darcy-scale reactive transport modeling would enable generating equivalent, large-scale flow and reaction functions. Incorporation of the effects of small-scale heterogeneities by implementing this upscaling framework would help constrain uncertainties in predicting field injection behaviors.

6. Conclusions

This work combines experimental and numerical approaches to quantify calcite dissolution and its effect on the flow behavior of limestone reacted with acidic fluids. The main conclusions drawn from this study are as follows

(1) A 3D Darcy-scale reactive transport model considering pore space heterogeneities solely on the permeability distribution can satisfactorily reproduce chemically-driven porosity

changes and dissolution patterns in the cores. Model results could be quantitatively improved by refining numerical mesh and using more accurate models for approximating the initial distribution and evolution of reactive surface area.

(2) Proper porosity-permeability correlations could impose a primary control on the model ability to capture the transition between different dissolution patterns in dissolving carbonate rocks.

(3) The small change in porosity in the form of compact dissolution in the case of HCl injection could be effectively simulated using the classical Kozeny-Carman relationship (with n_{grid} = 3), resulting in a stable dissolution front due to the complete dissociation of the strong acid. Yet, the applicability of this relationship to capture the effect of the strong acid on limestone over longer periods when we have larger porosity increases requires further investigation.

(4) A large $n_{grid} \approx 15$ in the power-law porosity-permeability relationship is required to capture the substantial porosity increase in the form of a wormhole during CO_2-saturated injection, where partial dissociation of the weak carbonic acid and its buffering effect cause the fast propagation of the dissolution front along the core.

(5) The extent of permeability evolution is found to be highly scale-dependent with n_{core} in the power-law porosity-permeability relationship reaching a value as high as 27.6 for the bulk behavior of the core.

(6) The proposed continuum-scale modeling framework successfully captures the dynamics of acidic fluid-rock interactions and could provide a promising tool for exploring reactive transport at larger scales, contingent upon appropriate calibration.

Acknowledgments

This work has received funding from the European Union's Horizon 2020 Research and Innovation Programme 2014-2018 under agreement No. 847593, specifically from the WP MAGIC. J.C. and J.M.S. acknowledge funding from the Catalan Government through project 2021 SGR 00308. I.R.K. and V.V. acknowledge support by the PCI2021-122077-2B project (www.easygeocarbon.com) funded by MCIN/AEI/10.13039/501100011033 and the European Union NextGenerationEU/PRTR. I.R.K. also received funding from the Engineering and Physical Sciences Research Council through the UKRI Postdoc Guarantee Award THMC4CCS [Grant number EP/X026019/1]. V.V. acknowledges funding from the Spanish Ministry of Science and Innovation through the project HydroPore (PID2019-106887GB-C32). IDAEA-CSIC is a Centre of Excellence Severo Ochoa (Spanish Ministry of Science and Innovation, Project CEX2018-000794-S funded by MCIN/AEI/10.13039/501100011033). This research has also been carried out within the framework of the activities of the Spanish Government through the "Maria de Maeztu Centre of Excellence" accreditation to IMEDEA (CSIC-UIB) (CEX2021-001198).

Data availability statement

We have used the CrunchFlow reactive transport code for numerical simulations in this study. The source files of the code can be found on GitHub from the developer (https://github.com/cisteefel/crunchtope). The input files to simulate the problem using the CrunchFlow code are publicly available at the institutional repository Digital.CSIC, which practices FAIR principles (http://hdl.handle.net/10261/351092). Matlab scripts developed to extract rock permeability maps from micro-CT images are also publicly available at the Digital.CSIC repository (http://hdl.handle.net/10261/284837).

Appendix A

Table A1 pH and chemical composition of the input solutions and equilibrium and kinetic parameters related to calcite dissolution. Note that the calcite dissolution rate is pH-dependent and described by two parallel (simultaneous) rate laws (Palandri and Kharaka, 2004; Xu et al., 2012).

	L_1-CO_2-28	***L_2-HCl-28***
calcite volume fraction	0.762	0.715
input solution		
pH	3.13	3.13, 2.66
Total concentrations (mol kg^{-1})		
$[Cl^-]$	0.0	7.58×10^{-4}, 2.1×10^{-3}
$[CO_2(aq)]$	1.03	6.6×10^{-6} equilibrium with atmospheric CO_2
reaction	$CaCO_3(s) + H^+ \Leftrightarrow Ca^{2+} + HCO_3^-$	
Equilibrium constants		
	p = 100 bar	p = 1 bar
log K_{eq} (60 °C)	-8.78	-8.88
Kinetic parameters	acidic conditions	neutral conditions
log k_{25} (25 °C) (mol m^2mineral s^{-1})	-0.3	-5.81
Ea (kcal mol^{-1})	3.44	5.62
$a_{H^+}^{n_{H^+}}$	1.0	-
m_1	3.0	3.0
m_2	1.0	1.0

744 **Table A2** Data of numerical discretization and flow properties of the different zones used in the

745 3D numerical simulations

	L_1-CO_2-28	***L_2-HCl-28***
sample dimensions		
diameter (mm)	25	25
length (mm)	44	78
discretization		
total number of cells in X - cell size (mm)	20 – 1.25	20 – 1.25
total number of cells in Y - cell size (mm)	20 – 1.25	20 – 1.25
total number of cells in Z - cell size (mm)	21 – 2.2	23 – 3.54
zones		
Pont du Gard core	limestone	limestone
initial average permeability (m^2)	2.54×10^{-14}	3.76×10^{-14}
initial average porosity (%)	23.8	28.5
non-reactive surrounding	calcite	calcite
initial permeability (m^2)	1.0×10^{-22}	1.0×10^{-22}
initial average porosity (%)	5.8	5.8
high permeability inlet	calcite	calcite
initial permeability (m^2)	1.0×10^{-9}	1.0×10^{-9}
initial average porosity (%)	23.8	28.5

746

747 ## References

748 Al-Khulaifi, Y., Lin, Q., Blunt, M.J. and Bijeljic, B., 2018. Reservoir-condition pore-scale imaging
749 of dolomite reaction with supercritical CO_2 acidified brine: Effect of pore-structure on reaction
750 rate using velocity distribution analysis. Int. J. Greenhouse Gas Control 68, 99-111.
751 https://doi.org/10.1016/j.ijggc.2017.11.011

752 Beckingham, L.E., Peters, C.A., Um, W., Jones, K.W., Lindquist, W.B., 2013. 2D and 3D imaging
753 resolution trade-offs in quantifying pore throats for prediction of permeability. Adv. Water Resour.
754 62, 1-12. https://doi.org/10.1016/j.advwatres.2013.08.010

755 Beckingham, L.E., Mitnick, E.H., Steefel, C.I., Zhang, S., Voltolini, M., Swift, A.M., Yang, L.,
756 Cole, D.R., Sheets, J.M., Ajo-Franklin, J.B., DePaolo, D.J., 2016. Evaluation of mineral reactive

surface area estimates for prediction of reactivity of a multi-mineral sediment. Geochim. Cosmochim. Acta 188, 310-329. https://doi.org/10.1016/j.gca.2016.05.040

Beckingham, L.E., 2017. Evaluation of macroscopic porosity-permeability relationships in heterogeneous mineral dissolution and precipitation scenarios. Water Resour. Res. 53(12), 10217-10230. https://doi.org/10.1002/2017WR021306

Brantley, S.L., Kubicki, J.D., White, A.F. eds., 2008. Kinetics of water-rock interaction. https://doi.org/10.1007/978-0-387-73563-4

Brosse, É., Magnier, C. and Vincent, B., 2005. Modeling fluid-rock interaction induced by the percolation of CO2-enriched solutions in core samples: the role of reactive surface area. Oil Gas Sci. Technol. 60(2), 287-305. https://doi.org/10.2516/ogst:2005018

Bernadiner, M.G., Thompson, K.E., Fogler, H.S., 1992. Effect of foams used during carbonate acidizing. SPE Prod. Eng. 7(04):350-6. https://doi.org/10.2118/21035-PA

Cama, J., Soler, J.M., Ayora, C., 2019. Acid water–rock–cement interaction and multicomponent reactive transport modeling. Rev. Mineral. Geochem. 85(1), 459-498. https://doi.org/10.2138/rmg.2018.85.15

Cavanagh, A. Ringrose, P., 2011. Simulation of CO_2 distribution at the In Salah storage site using high-resolution field-scale models. Energy Procedia, 4, 3730-3737.

Cohen C.E., Ding, D., Quintard, M., Bazin, B., 2008. From pore scale to wellbore scale: Impact of geometry on wormhole growth in carbonate acidization. Chem. Eng. Sci. 63(12), 3088-3099. https://doi.org/10.1016/j.ces.2008.03.021

Darcy, H., 1856. Les fontaines publiques de la ville de Dijon: Exposition et application des principes à suivre et des formules à employer dans les questions de distribution d'eau: Ouvrage terminé par un appendice relatif aux fournitures d'eau de plusieurs villes, au filtrage des eaux et à la fabrication des tuyaux de fonte, de plomb, de tôle et de bitume.

Daccord, G., Touboul, E., Lenormand, R., 1989. Carbonate acidizing: toward a quantitative model of the wormholing phenomenon. SPE Prod. Eng. 4(01), 63-8. https://doi.org/10.2118/16887-PA

Dávila, G., Cama, J., Luquot, L., Soler, J.M., Ayora, C., 2017. Experimental and modeling study of the interaction between a crushed marl caprock and CO2-rich solutions under different pressure and temperature conditions. Chem. Geol. 448, 26-42. https://doi.org/10.1016/j.chemgeo.2016.10.034

Dávila, G., Dalton, L., Crandall, D.M., Garing, C., Werth, C.J. and Druhan, J.L., 2020. Reactive alteration of a Mt. Simon Sandstone due to CO_2-rich brine displacement. Geochim. Cosmochim. Acta 271, 227-247. https://doi.org/10.1016/j.gca.2019.12.015

De Paulo Ferreira, L., Surmas, R., Tonietto, S.N., Da Silva, M.A.P., Peçanha, R.P., 2020. Modeling reactive flow on carbonates with realistic porosity and permeability fields. Adv. Water Resour. 139, 103564. https://doi.org/10.1016/j.advwatres.2020.103564

Ellis, B., Peters, C., Fitts, J., Bromhal, G., McIntyre, D., Warzinski, R., Rosenbaum, E., 2011. Deterioration of a fractured carbonate caprock exposed to CO_2-acidified brine flow. Greenhouse Gases Sci. Technol. 1(3), 248-260. https://doi.org/10.1002/ghg.25

Fredd, C.N., Fogler, H.S., 1998. Influence of transport and reaction on wormhole formation in porous media. Fluid Mech. Transp. Phenomena 4, 1933-1949. https://doi.org/10.1002/aic.690440902

Fredd, C.N., 2000. Dynamic model of wormhole formation demonstrates conditions for effective skin reduction during carbonate matrix acidizing. SPE conference. https://doi.org/10.2118/59537-MS

Fitch, P.J., Lovell, M.A., Davies, S.J., Pritchard, T. and Harvey, P.K., 2015. An integrated and quantitative approach to petrophysical heterogeneity. Mar. Pet. Geol. 63, 82-96. https://doi.org/10.1016/j.marpetgeo.2015.02.014

Garcia-Rios, M., Luquot, L., Soler, J.M. and Cama, J., 2015. Influence of the flow rate on dissolution and precipitation features during percolation of CO_2-rich sulfate solutions through fractured limestone samples. Chem. Geol. 414, 95-108. https://doi.org/10.1016/j.chemgeo.2015.09.005

Garcia-Rios, M., Luquot, L., Soler, J.M., Cama, J., 2017. The role of mineral heterogeneity on the hydrogeochemical response of two fractured reservoir rocks in contact with dissolved CO_2. Appl Geochem 84, 202-217. https://doi.org/10.1016/j.apgeochem.2017.06.008

Garing, C., Gouze, P., Kassab, M., Riva, M., Guadagnini, A., 2015. Anti-correlated porosity–permeability changes during the dissolution of carbonate rocks: experimental evidences and modeling. Transp. Porous Media 107(2), 595-621. https://doi.org/10.1007/s11242-015-0456-2

Gaus, I., 2010. Role and impact of CO_2–rock interactions during CO_2 storage in sedimentary rocks. Int. J. Greenhouse Gas Control 4(1), 73-89. https://doi.org/10.1016/j.ijggc.2009.09.015

Gautier, J.M., Oelkers, E.H., Schott, J., 2001. Are quartz dissolution rates proportional to BET surface areas? Geochim. Cosmochim. Acta 65(7), 1059-1070. https://doi.org/10.1016/S0016-7037(00)00570-6

Golfier, F., Bazin, B., Zarcone, C., Lernormand, R., Lasseux, D., Quintard, M., 2001. Acidizing carbonate reservoirs: numerical modeling of wormhole propagation and comparison to experiments. SPE conference. https://doi.org/10.2118/68922-MS

Golfier, F., Zarcone, C., Bazin, B., Lenormand, R., Lasseux, D., Quintard, M., 2002. On the ability of a Darcy-scale model to capture wormhole formation during the dissolution of a porous medium. J Fluid Mech. 457, 213-54. https://doi.org/10.1017/S0022112002007735

Gouze, P., Luquot, L., 2009. X-ray microtomography characterization of porosity, permeability, and reactive surface changes during dissolution. J Contam. Hydrol. 120-121, 45-55. https://doi.org/10.1016/j.jconhyd.2010.07.004

Gouze, P., Luquot, L., 2011. X-ray microtomography characterization of porosity, permeability and reactive surface changes during dissolution. J Contam Hydrol 120-121, 45-55. https://doi.org/10.1016/j.jconhyd.2010.07.004

Gray, F., Anabaraonye, B., Shah, S., Boek, E., Crawshaw, J., 2018. Chemical mechanisms of dissolution of calcite by HCl in porous media: Simulations and experiment. Adv. Water Resour. 1(121), 369-87.

Gray, F., Anabaraonye, B.U., Crawshaw, J.P. and Boek, E.S., 2021. Pore-scale dissolution mechanisms in calcite-CO_2-brine systems: the impact of non-linear reaction kinetics and coupled

ion transport. Geochim. Cosmochim. Acta 305, 323-338. https://doi.org/10.1016/j.gca.2021.04.002

Gray, K., 2015. Carbon Storage Atlas (No. DOE-SSEB-42590-120). Southern States Energy Board, Peachtree Corners, GA (United States). https://doi.org/10.2172/1814016

Hao, Y., Smith, M., Sholokhova, Y., Carroll, S., 2013. CO_2-induced dissolution of low permeability carbonates. Part II: Numerical modeling of experiments. Adv. Water Resour. 62, 388-408. https://doi.org/10.1016/j.advwatres.2013.09.009

Hao, Y., Smith, M.M., Carroll, S.A., 2019. Multiscale modeling of CO_2-induced carbonate dissolution: From core to meter scale. Int. J. Greenhouse Gas Control 88, 272-289. https://doi.org/10.1016/j.ijggc.2019.06.007

Hommel, J., Coltman, E. Class, H., 2018. Porosity–permeability relations for evolving pore space: a review with a focus on (bio-) geochemically altered porous media. Transp. Porous Media 124(2), 589-629. https://doi.org/10.1007/s11242-018-1086-2

Izgec, O., Demiral, B., Bertin, H. and Akin, S., 2008. CO_2 injection into saline carbonate aquifer formations II: Comparison of numerical simulations to experiments. Transp. Porous Media 73(1), 57-74. https://doi.org/10.1007/s11242-007-9160-1

Jackson, S.J., Lin, Q., Krevor, S., 2020. Representative elementary volumes, hysteresis, and heterogeneity in multiphase flow from the pore to the continuum scale. Water Resour. Res. 56(6), p.e2019WR026396. https://doi.org/10.1029/2019WR026396

Kalia, N. and Balakotaiah, V., 2009. Effect of medium heterogeneities on the reactive dissolution of carbonates. Chem. Eng. Sci. 64(2), 376-390. https://doi.org/10.1016/j.ces.2008.10.026

Kane, A.V., 1979. Performance review of a large-scale CO_2-WAG enhanced recovery project, SACROC Unit Kelly-Snyder Field. J. Pet. Technol. 31(02), 217-231.

Kang, Q., Zhang, D. Chen, S., 2003. Simulation of dissolution and precipitation in porous media. J. Geophys. Res. Solid Earth 108(B10). https://doi.org/10.1029/2003JB002504

Khather, M., Yekeen, N., Al-Yaseri, A., Al-Mukainah, H., Giwelli, A., Saeedi, A., 2022. The impact of wormhole generation in carbonate reservoirs on CO_2-WAG oil recovery. J. Petrol. Sci. Eng. 212, p.110354. https://doi.org/10.1016/j.petrol.2022.110354

Lai, P., Moulton, K., Krevor, S., 2015. Pore-scale heterogeneity in the mineral distribution and reactive surface area of porous rocks. Chem. Geol. 411, 260-273. https://doi.org/10.1016/j.chemgeo.2015.07.010

Leger, M., Roubinet, D., Jamet, M., Luquot, L., 2022. Impact of hydro-chemical conditions on structural and hydro-mechanical properties of chalk samples during dissolution experiments. Chem. Geol. 594, 120763. https://doi.org/10.1016/j.chemgeo.2022.120763

Li, L., Steefel, C.I., Yang, L., 2008. Scale dependence of mineral dissolution rates within single pores and fractures. Geochim. Cosmochim. Acta 72(2), 360-377. https://doi.org/10.1016/j.gca.2007.10.027

Ling, B., Sodwatana, M., Kohli, A., Ross, C.M., Jew, A., Kovscek, A.R., Battiato, I., 2022. Probing multiscale dissolution dynamics in natural rocks through microfluidics and compositional analysis. PNAS 119(32), e2122520119. https://doi.org/10.1073/pnas.2122520119

Liu, P., Huang, C., Jia, L., Ji, W., Zhang, Z., Zhang, K., 2022. Numerical simulation of the wormhole propagation in fractured carbonate rocks during acidization using a thermal-hydrologic-mechanics-chemical coupled model. Water 14(24), 4117. https://doi.org/10.3390/w14244117

Liu, N., Liu, M., 2016. Simulation and analysis of wormhole propagation by VES acid in carbonate acidizing. J. Pet. Sci. Eng. 138, 57-65. https://doi.org/10.1016/j.petrol.2015.12.011

Luo, S., Xu, R., Jiang, P., 2012. Effect of reactive surface area of minerals on mineralization trapping of CO 2 in saline aquifers. Pet. Sci. 9, 400-407. https://doi.org/10.1007/s12182-012-0224-7

Luquot, L., Gouze, P., 2009. Experimental determination of porosity and permeability changes induced by injection of CO_2 into carbonate rocks. Chem. Geol. 265(1-2),148-59. https://doi.org/10.1016/j.chemgeo.2009.03.028

Luquot, L., Rodriguez, O., Gouze, P., 2014. Experimental characterization of porosity structure and transport property changes in limestone undergoing different dissolution regimes. Transp. Porous Media 101, 507-532. https://doi.org/10.1007/s11242-013-0257-4

Lüttge, A., Winkler, U., Lasaga, A.C., 2003. An interferometric study of dolomite dissolution: a new conceptual model for mineral dissolution. Geochim. Cosmochim. Acta 67 (6), 1099–1116. https://doi.org/10.1016/S0016-7037(02)00914-6

Mahmoodi, A., Javadi, A. Sola, B.S., 2018. Porous media acidizing simulation: New two-phase two-scale continuum modeling approach. J. Pet. Sci. Eng. 166, 679-692. https://doi.org/10.1016/j.petrol.2018.03.072

Manoorkar, S., Jackson, S.J., Krevor, S., 2021. Observations of the impacts of millimeter-to centimeter-scale heterogeneities on relative permeability and trapping in carbonate rocks. Water Resour. Res. 57(4), p.e2020WR028597. https://doi.org/10.1029/2020WR028597

McLeod, H.O., 1984. Matrix acidizing. J. Pet. Technol. 36(12), 2055-2069. https://doi.org/10.2118/13752-PA

Menke, H.P., Bijeljic, B., Andrew, M.G., Blunt, M.J., 2015. Dynamic three-dimensional pore-scale imaging of reaction in a carbonate at reservoir conditions. Environ. Sci. Technol. 49(7), 4407-4414. https://doi.org/10.1021/es505789f

Menke, H.P., Andrew, M.G., Blunt, M.J., Bijeljic, B., 2016. Reservoir condition imaging of reactive transport in heterogeneous carbonates using fast synchrotron tomography—Effect of initial pore structure and flow conditions. Chem. Geol. 428, pp.15-26. https://doi.org/10.1016/j.chemgeo.2016.02.030

Menke, H.P., Bijeljic, B., Blunt, M.J., 2017. Dynamic reservoir-condition microtomography of reactive transport in complex carbonates: Effect of initial pore structure and initial brine pH. Geochim. Cosmochim. Acta 204, 267-285. https://doi.org/10.1016/j.gca.2017.01.053

Menke, H.P., Maes, J., Geiger, S., 2021. Upscaling the porosity–permeability relationship of a microporous carbonate for Darcy-scale flow with machine learning. Sci. Rep.11(1), 2625. https://doi.org/10.1038/s41598-021-82029-2

Metz, B., Davidson, O., De Coninck, H., Loos, M., Meyer, L., 2005. Carbon Dioxide Capture and Storage. Summary for Policymakers. IPCC.

Molins, S., Trebotich, D., Yang, L., Ajo-Franklin, J.B., Ligocki, T.J., Shen, C., Steefel, C.I., 2014. Pore-scale controls on calcite dissolution rates from flow-through laboratory and numerical experiments. Environ. Sci. Technol. 48(13), 7453-60. https://doi.org/10.1021/es5013438

Mostaghimi, P. Mahani, H., 2010. A quantitative and qualitative comparison of coarse-grid-generation techniques for modeling fluid displacement in heterogeneous porous media. SPE Reservoir Evaluation & Engineering, 13(01), 24-36. https://doi.org/10.2118/118712-PA

Noiriel, C., Gouze, P. and Bernard, D., 2004. Investigation of porosity and permeability effects from microstructure changes during limestone dissolution. Geophys. Res. Lett. 31(24). https://doi.org/10.1029/2004GL021572

Noiriel, C., Bernard, D., Gouze, P., Thibault, X., 2005. Hydraulic properties and microgeometry evolution accompanying limestone dissolution by acidic water. Oil Gas Sci. Technol. Rev. IFP 60, 177-192. https://doi.org/10.2516/ogst:2005011

Noiriel, C., Luquot, L., Madé, B., Raimbault, L., Gouze, P. van Der Lee, J., 2009. Changes in reactive surface area during limestone dissolution: An experimental and modeling study. Chem. Geol. 265(1-2), 160-170. https://doi.org/10.1016/j.chemgeo.2009.01.032

Noiriel, C., Seigneur, N., Le Guern, P., Lagneau, V., 2021. Geometry and mineral heterogeneity controls on precipitation in fractures: An X-ray micro-tomography and reactive transport modeling study. Adv. Water Resour. 152, 103916. https://doi.org/10.1016/j.advwatres.2021.103916

Noiriel, C. Soulaine, C., 2021. Pore-scale imaging and modelling of reactive flow in evolving porous media: Tracking the dynamics of the fluid–rock interface. Transp. Porous Media, 140(1),181-213. https://doi.org/10.1007/s11242-021-01613-2

Oelkers, E.H., 2018. Physical and chemical properties of rocks and fluids for chemical mass transport calculations. Reactive transport in porous media 17:131-192. https://doi.org/10.1515/9781501509797-006

Omrani, S., Ghasemi, M., Mahmoodpour, S., Shafiei, A., Rostami, B., 2022. Insights from molecular dynamics on CO_2 diffusion coefficient in saline water over a wide range of temperatures, pressures, and salinity: CO_2 geological storage implications. J. Mol. Liq. 345, 117868. https://doi.org/10.1016/j.molliq.2021.117868

Ortoleva, P., Merino, E., Moore, C., Chadam, J., 1987. Geochemical self-organization I; reaction-transport feedbacks and modeling approach. Am. J. Sci. 287(10), pp.979-1007.

Ott, H., de Kloe, K., Van Bakel, M., Vos, F., Van Pelt, A., Legerstee, P., Bauer, A., Eide, K., Van Der Linden, A., Berg, S., Makurat, A., 2012. Core-flood experiment for transport of reactive fluids in rocks. Rev. Sci. Instrum. 83(8). https://doi.org/10.1063/1.4746997

Ott, H., Oedai, S., 2015. Wormhole formation and compact dissolution in single-and two-phase CO_2-brine injections. Geophys. Res. Lett. 2(7), 2270-6. https://doi.org/10.1002/2015GL063582

Panga, M.K., Ziauddin, M. and Balakotaiah, V., 2005. Two-scale continuum model for simulation of wormholes in carbonate acidization. AIChE journal, 51(12), pp.3231-3248. https://doi.org/10.1002/aic.10574

Park, B.H. and Lee, K.K., 2021. Evaluating anisotropy ratio of thermal dispersivity affecting geometry of plumes generated by aquifer thermal use. J. Hydrol. 602, 126740. https://doi.org/10.1016/j.jhydrol.2021.126740

Parkhurst, D.L. and Appelo, C.A.J., 2013. Description of input and examples for PHREEQC version 3—a computer program for speciation, batch-reaction, one-dimensional transport, and inverse geochemical calculations. US geological survey techniques and methods, 6(A43), p.497. https://pubs.usgs.gov/tm/06/a43/

Palandri, J.L. Kharaka, Y.K., 2004. A compilation of rate parameters of water-mineral interaction kinetics for application to geochemical modeling. Science for a changing world. U.S. Geol. Surv. Open File Report 2004-1068. http://pubsdata.usgs.gov/pubs/of/2004/1068/

Pereira Nunes, J.P., Bijeljic, B., Blunt, M.J., 2016. Pore-space structure and average dissolution rates: A simulation study. Water Resour. Res. 52(9), 7198-7212. https://doi.org/10.1002/2016WR019313

Qin, F. Beckingham, L.E., 2021. The impact of mineral reactive surface area variation on simulated mineral reactions and reaction rates. Appl. Geochem. 124, 104852. https://doi.org/10.1016/j.apgeochem.2020.104852

Raj, N., Pal, T.V., 2014. Enhancing efficiency of HCl-based stimulating fluids by creating in-situ carbonic acid using nickel nanoparticles. IPTC Conference. https://doi.org/10.2523/IPTC-17814-MS

Randi, A., Sterpenich, J., Thiéry, D., Kervévan, C., Pironon, J., Morlot, C., 2017. Experimental and numerical simulation of the injection of a CO_2 saturated solution in a carbonate reservoir: application to the CO_2-DISSOLVED concept combining CO_2 geological storage and geothermal heat recovery. Energy Procedia 114, 2942-2956. https://doi.org/10.1016/j.egypro.2017.03.1423

Reimus, P., Pohll, G., Mihevc, T., Chapman, J., Haga, M., Lyles, B., Kosinski, S., Niswonger, R., Sanders, P., 2003. Testing and parameterizing a conceptual model for solute transport in a fractured granite using multiple tracers in a forced-gradient test. Water Resour. Res. 39(12). https://doi.org/10.1029/2002WR001597

Rohmer, J., Pluymakers, A., Renard, F., 2016. Mechano-chemical interactions in sedimentary rocks in the context of CO_2 storage: Weak acid, weak effects? Earth Sci. Rev. 157, 86–110. https://doi.org/10.1016/j.earscirev.2016.03.009

Sahimi, M., 2011. Flow and transport in porous media and fractured rock: from classical methods to modern approaches. John Wiley & Sons. DOI:10.1002/9783527636693

Salehikhoo, F. Li, L., 2015. The role of magnesite spatial distribution patterns in determining dissolution rates: When do they matter? Geochim. Cosmochim. Acta 155, 107-121. https://doi.org/10.1016/j.gca.2015.01.035

Smith, L., Chapman, D.S., 1983. On the thermal effects of groundwater flow: 1. Regional scale systems. J. Geophys. Res. Solid Earth 88(B1), 593-608. https://doi.org/10.1029/JB088iB01p00593

Smith, M.M., Sholokhova, Y., Hao, Y., Carroll, S.A., 2013. CO_2-induced dissolution of low permeability carbonates. Part I: Characterization and experiments. Adv. Water Resour. 62, 370-87. https://doi.org/10.1016/j.advwatres.2013.09.008

Smith, M.M., Hao, Y., Carroll, S.A., 2017. Development and calibration of a reactive transport model for carbonate reservoir porosity and permeability changes based on CO_2 core-flood

experiments. Int. J. Greenhouse Gas Control 57, 73–88. https://doi.org/10.1016/j.ijggc.2016.12.004

Snippe, J., Gdanski, R., Ott, H., 2017. Multiphase modeling of wormhole formation in carbonates by the injection of CO_2. Energy Procedia 114, 2972-84. https://doi.org/10.1016/j.egypro.2017.03.1426

Snippe, J., Berg, S., Ganga, K., Brussee, N., Gdanski, R., 2020. Experimental and numerical investigation of wormholing during CO_2 storage and water alternating gas injection. Int. J. Greenhouse Gas Control 94, 102901. https://doi.org/10.1016/j.ijggc.2019.102901

Soulaine, C., Roman, S., Kovscek, A., Tchelepi, H.A., 2018. Pore-scale modeling of multiphase reactive flow: application to mineral dissolution with production of CO_2. J. Fluid Mech. 855, 616-645. https://doi.org/10.1017/jfm.2018.655

Steefel, C.I., DePaolo, D.J., Lichtner, P.C., 2005. Reactive transport modeling: An essential tool and a new research approach for the Earth sciences. Earth Planet. Sci. Lett. 240(3-4), 539-558. https://doi.org/10.1016/j.epsl.2005.09.017

Steefel, C.I., 2008. Geochemical kinetics and transport. Kinetics of water-rock interaction, 545-589. https://doi.org/10.1007/978-0-387-73563-4_11

Steefel, C.I., Appelo, C.A.J., Arora, B., Jacques, D., Kalbacher, T., Kolditz, O., Lagneau, V., Lichtner, P.C., Mayer, K.U., Meeussen, J.C.L., Molins, S., 2015. Reactive transport codes for subsurface environmental simulation. Comput. Geosci. 19, 445-478. https://doi.org/10.1007/s10596-014-9443-x

Steefel, C.I., Molins, S., 2016. CrunchFlow. Software for modeling multicomponent reactive flow and transport. User's manual. Lawrence Berkeley National Laboratory, Berkeley.

Steefel, C.I., Appelo, C.A.J., Arora, B., Jacques, D., Kalbacher, T., Kolditz, O., Lagneau, V., Lichtner, P.C., Mayer, K.U., Meeussen, J.C.L., Molins, S., 2015. Reactive transport codes for subsurface environmental simulation. Comput. Geosci. 19(3), 445-478. https://doi.org/10.1007/s10596-014-9443-x

Szymczak, P., Ladd, A.J.C., 2009. Wormhole formation in dissolving fractures. J Geophys Res. Solid Earth 114, B06203. https://doi.org/10.1029/2008JB006122

Szymczak, P. Ladd, A.J., 2011. Instabilities in the dissolution of a porous matrix. Geophys. Res. Lett. 38(7). https://doi.org/10.1029/2011GL046720

Tangirala, S.K., Ziegler, M., Makhnenko, R.Y., Vilarrasa, V., 2024. Field-scale hydro-mechanical simulation of a novel monitoring system for the CO_2 Long-Term Periodic Injection Experiment (CO2LPIE) at the Mont Terri rock laboratory. In 1st Caprock Integrity & Gas Storage Symposium 2024 (p. 117). https://doi.org/10.60695/swisstopo-25012024

Tewes, F., Boury, F., 2005. Formation and rheological properties of the supercritical CO_2–water pure interface. J. Phys. Chem. B 109(9), 3990–3997. https://doi.org/10.1021/jp046019w

Trabucchi, M., Garcia, D.F. and Carrera, J., 2023. Visualizing and evaluating wormholes formation dynamics under flow competition in an intermediate-scale dissolution experiment. Sci. Total Environ. 867, 160977. https://doi.org/10.1016/j.scitotenv.2022.160977

Vafaie, A., Soler, J.M., Cama, J., Kivi, I.R., Vilarrasa, V., 2022. [CODE] A MATLAB code for the digitized reconstruction of the rock porosity distribution from Computed Tomography (CT) images. http://hdl.handle.net/10261/284837

Vafaie, A., Cama, J., Soler, J.M., Kivi, I.R., Vilarrasa, V., 2023a. Chemo-hydro-mechanical effects of CO_2 injection on reservoir and seal rocks: A review on laboratory experiments. Renewable Sustainable Energy Rev. 178, 113270. https://doi.org/10.1016/j.rser.2023.113270

Vafaie, A., Cama, J., Soler, J.M., Grgic, D., Vilarrasa, V., 2023b. Chemo-hydro-mechanical effects of CO_2 injection into a permeable limestone. Int. J. Coal. Geol. 278, 104359. https://doi.org/10.1016/j.coal.2023.104359

Vafaie, A., Soler, J.M., Cama, J., Kivi, I.R., Vilarrasa, V., 2024. Numerical models for simulating reactive flow of HCl and CO_2-rich water in cm-scale limestone samples [Dataset]. DIGITAL.CSIC. https://doi.org/10.20350/digitalCSIC/16167

Vafaie, A., Soler, J.M., Cama, J., Kivi, I.R., Vilarrasa, V., 2024. A MATLAB approach for developing digital rock models of heterogeneous limestones for reactive transport modeling. Geologica Acta, 22. https://doi.org/10.1344/GeologicaActa2024.22.3

Vanorio, T., Mavko, G., 2011. Laboratory measurements of the acoustic and transport properties of carbonate rocks and their link with the amount of microcrystalline matrix. Geophysics 76, E105–E115.https://doi.org/10.1190/1.3580632

Vialle, S., Dvorkin, J. and Mavko, G., 2013. Implications of pore microgeometry heterogeneity for the movement and chemical reactivity of CO_2 in carbonates. Geophysics, 78(5), pp.L69-L86. https://doi.org/10.1190/geo2012-0458.1

Vialle, S., Contraires, S., Zinzsner, B., Clavaud, J.B., Mahiouz, K., Zuddas, P., Zamora , M., 2014. Percolation of CO_2-rich fluids in a limestone sample: Evolution of hydraulic, electrical, chemical, and structural properties. J. Geophys. Res. Solid Earth 119, 2828-2847. https://doi.org/10.1002/2013JB010656

Voltolini, M., Ajo-Franklin, J., 2019. The effect of CO_2-induced dissolution on flow properties in Indiana limestone: An in situ synchrotron X-ray micro-tomography study. Int. J. Greenhouse Gas Control 82, 38-47. https://doi.org/10.1016/j.ijggc.2018.12.013

Wolery, T.J., Jackson, K.J., Bourcier, W.L., Bruton, C.J., Viani, B.E., Knauss, K.G., Delany, J.M., 1990. Current Stetus of the EQ3/6 Software Package for Geochemical Modeling. In: Chemical Modeling of Aqueous Systems II, 104–116. DOI: 10.1021/bk-1990-0416.ch008

Xu, J., Fan, C. and Teng, H.H., 2012. Calcite dissolution kinetics in view of Gibbs free energy, dislocation density, and pCO_2. Chem. Geol. 322, 11-18. https://doi.org/10.1016/j.chemgeo.2012.04.019

Ziegler, M., Fritsche, T., Czerner, S., 2024. A borehole modular multi-sensor monitoring system (MMMS). In 1st Caprock Integrity & Gas Storage Symposium 2024 (p. 133). https://doi.org/10.60695/swisstopo-25012024

Supporting Information for

A 3D Darcy-scale reactive transport modeling of experimental wormhole formation in limestone under geological CO_2 storage conditions

Atefeh Vafaie[1*], Josep M. Soler[2], Jordi Cama[2], Iman R. Kivi[1], Victor Vilarrasa[3]

[1]Department of Earth Science and Engineering, Imperial College London, London, UK

[2]Institute of Environmental Assessment and Water Research, Spanish National Research Council (IDAEA-CSIC), Barcelona, Spain

[3]Mediterranean Institute for Advanced Studies (IMEDEA), Spanish National Research Council (CSIC), Esporles, Spain

[*]Corresponding author: Atefeh Vafaie (a.vafaie@imperial.ac.uk)

In the Supporting Information, we present (1) the equilibrium constants (log K_{eq}) and stoichiometric coefficients for equilibria in the solution for experiments ***L_1-CO_2-28*** and ***L_2-HCl-28*** and (2) details of the image processing workflow used in this study to construct 3D permeability maps of the limestone cores.

1. Equilibrium constants (log *Keq*) and stoichiometric coefficients

The stoichiometric coefficients and log K_{eq} values for the different homogeneous (speciation) reactions are listed below in Table S1.

Table S1. Equilibrium constants (log K_{eq}) and stoichiometric coefficients for equilibria in solution for experiments *L_1-CO_2-28* and *L_2-HCl-28*. Reactions are written as the destruction of 1mol of the species in the first column

Species		**log K_{eq}**	**Stoichiometric coefficient**			
L_1-CO_2-28	***L_2-HCl-28***	**60 °C**	Ca^{2+}	HCO_3^-	H^+	Cl^-
CO_2 (aq)	CO_2 (aq)	-6.268	0	1	1	0
$CaCO_3$ (aq)	$CaCO_3$ (aq)	6.452	1	1	-1	0
$CaHCO_3^+$	$CaHCO_3^+$	-1.159	1	1	0	0
$CaOH^+$	$CaOH^+$	12.850	1	0	-1	0
CO_3^{2-}	CO_3^{2-}	10.130	0	1	-1	0
OH^-	OH^-	13.027	0	0	-1	0
	HCl (aq)	-0.688	0	0	1	1
	$CaCl^+$	0.589	1	0	0	1
	$CaCl_2$(aq)	0.629	1	0	0	2

2. Image processing workflow

The image processing workflow used in this work consists of five main steps. The first step includes the decomposition of the full-core µCT image into discrete rectangular cuboid (layers) sub-volumes along the axis of the specimens (z-direction). The number of sub-volumes here is equal to the number of grid cells in the z-direction. This decomposition significantly reduces the computational costs of processing large images. Equidistributed square-shaped gray-scale cross-section images are extracted from each sub-volume in the second step. To keep as much information as possible in continuum representations of the pore-scale heterogeneities, the imaging interval is set to a minimum value equal to the voxel resolution.

The third step segments images to obtain stacks of 2D binary images. The segmentation in our study relies on the exertion of a global threshold on the gray-level intensity histogram to differentiate between pores (intensities < threshold) and the solid mineral phase (intensities > threshold). We found that the widely used Otsu technique (Otsu, 1979) to find the threshold returns reliable representations of the key rock structural features. These processes were implemented in the open-access ImageJ software (Schneider et al., 2012).

The Otsu thresholding method was selected from several automatic algorithms designed to statistically determine optimal threshold values based on intensity histograms. This selection was made because the Otsu approach demonstrated a better ability to reproduce distinct structural features observed in grayscale images when converted to binary images all along the core. However, it is important to acknowledge that the choice of threshold values is prone to user perception and may slightly impact the porosity calculations (Iassonov et al., 2009). We do not here aim to go through a detailed investigation of these effects.

In the fourth step, the binarized 2D cross-section images are transcripted on the grid cells domain in each sub-volume. These images are then used to calculate the total porosity of grid cells belonging to the limestone core using

$$\phi = \frac{1}{N}\sum_{n=1}^{N}\frac{voxel_0}{voxel_0 + voxel_1} \quad (1)$$

where N is the number of slices and $voxel_0$ and $voxel_1$ count the number of pore (0) and solid-phase (1) pixels. It should be noticed that ϕ accounts for both connected and isolated pores. However, the contribution of the latter to the porosity of the Pont Du Gard Limestone is plausibly negligible, enabling a direct comparison with the bulk effective porosity measured independently. Yet, the slice-averaged porosity may underestimate the effective rock porosity due to the presence of pores smaller than the CT resolution. Assuming that the sub-resolution pores are uniformly distributed on an otherwise solid calcite background, the background porosity is increased in the last processing step in a way that reproduces realistic average rock porosity.

The last two steps of the workflow, i.e., reading 2D binarized images, projecting them onto the grid cells domain, and calculating and (optionally) modifying the porosity of grid cells, were implemented in MATLAB (Fig. S1, see https://github.com/AVafaie/Porosity-reconstruction-from-CT.git and Vafaie, et al., 2022 for a detailed explanation). The same workflow was implemented on image data sets of the chemically altered samples to interpret dissolution patterns (altered porosity map in Fig. 1 in the main manuscript) and make comparisons with model predictions on the continuum domain.

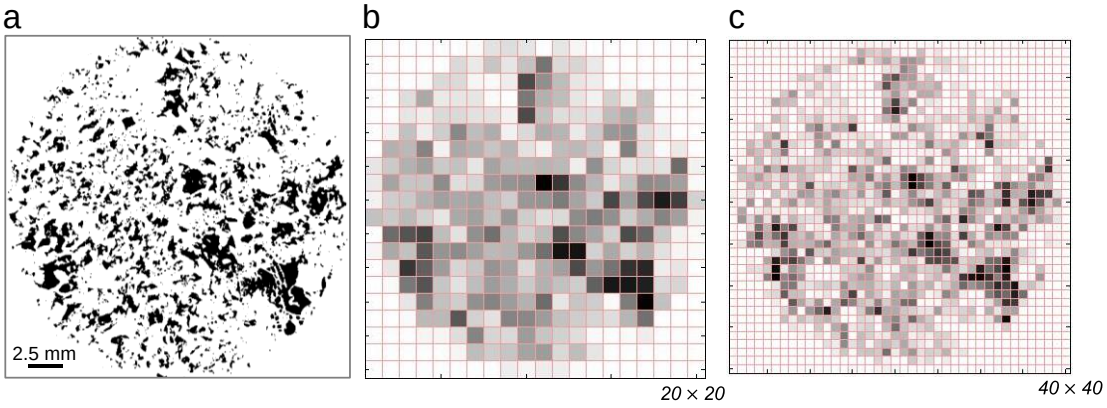

Fig. S1. 2D illustrations of a) a raw binary cross-section image, b) a reconstructed grid-based porosity map with a size of 20 × 20 cells, and c) a reconstructed grid-based porosity map with a size of 40 × 40 cells.

References for SI

Iassonov, P., Gebrenegus, T., Tuller, M., 2009. Segmentation of X-ray computed tomography images of porous materials: A crucial step for characterization and quantitative analysis of pore structures. Water Resour. Res. 45(9). https://doi.org/10.1029/2009WR008087

Otsu, N., 1979. A threshold selection method from gray-level histograms. IEEE Transactions on Systems, Man, and Cybernetics, 9(1), 62-66. 10.1109/TSMC.1979.4310076

Schneider, C.A., Rasband, W.S., Eliceiri, K.W., 2012. NIH Image to ImageJ: 25 years of image analysis. Nat. Methods, 9(7), 671-675. https://doi.org/10.1038/nmeth.2089

Vafaie, A., Soler, J.M., Cama, J., Kivi, I.R., Vilarrasa, V., 2022. [CODE] A MATLAB code for the digitized reconstruction of the rock porosity distribution from Computed Tomography (CT) images. http://hdl.handle.net/10261/284837